

1 Proteomic analysis of cell cycle progression in
2 asynchronous cultures, including mitotic subphases,
3 using PRIMMUS

4

5 Authors:

6

7 Tony Ly¹, Arlene Whigham², Rosemary Clarke², Alejandro Brenes-Murillo¹, Brett Estes³,
8 Patricia Wadsworth³ and Angus I. Lamond¹

9

10 Addresses:

- 11 1. Centre for Gene Regulation and Expression, School of Life Sciences, University of
12 Dundee, Dow Street, Dundee DD1 5EH, Scotland, United Kingdom
13 2. CAST Flow Cytometry Facility, School of Life Sciences, University of Dundee, Dow
14 Street, Dundee DD1 5EH, Scotland, United Kingdom
15 3. Department of Biology and Program in Molecular and Cellular Biology,
16 University of Massachusetts, Amherst, MA 01003, USA
17

18

19 Correspondence Details: t.ly@dundee.ac.uk, a.i.lamond@dundee.ac.uk

20

21 **Abstract (150/150 words)**

22 The temporal regulation of protein abundance and post-translational modifications is a
23 key feature of cell division. Recently, we analysed gene expression and protein
24 abundance changes during interphase under minimally perturbed conditions (Ly et al.
25 2014; Ly et al. 2015). Here we show that by using specific intracellular immunolabeling
26 protocols, FACS separation of interphase and mitotic cells, including mitotic subphases,
27 can be combined with proteomic analysis by mass spectrometry. Using this PRIMMUS
28 (PRoteomic analysis of Intracellular iMMUnolabeled cell Subsets) approach, we now
29 compare protein abundance and phosphorylation changes in interphase and mitotic
30 fractions from asynchronously growing human cells. We identify a set of 115
31 phosphorylation sites increased during G2, which we term 'early risers'. This set
32 includes phosphorylation of S738 on TPX2, which we show is important for TPX2
33 function and mitotic progression. Further, we use PRIMMUS to provide a proteome-
34 wide analysis of protein abundance remodeling between prophase, prometaphase and
35 anaphase.

36

37 **Introduction**

38

39

40

41

42

43

44

45

46

47

48

49

50

51

52

53

54

55

56

57

58

59

60

61

62

The mitotic cell division cycle is composed of four major phases, i.e., G1, S, G2

and M. The phases are defined by two major events during cell division: DNA replication

(S phase) and mitosis (M phase), with intervening gap phases (G1 and G2). The cell

cycle is driven by the expression of key proteins, called cyclins. Generally, cyclin

expression and function is restricted to specific cell cycle phases, driving temporally

ordered phosphorylation of key substrates by interacting with their kinase partners, the

cyclin dependent kinases (CDKs). Temporally regulated degradation of the cyclins

ensures that progression through the cell cycle is unidirectional. For example, cyclin A

expression increases during S-phase, reaching a maximum in mitosis. During

prometaphase, cyclin A is targeted for degradation by the anaphase promoting

complex/cyclosome (APC/C), a multiprotein E3 ubiquitin ligase, thus restricting cyclin

A-driven phosphorylation to S, G2 and early M-phase.

Mitosis can be further resolved into subphases (i.e. prophase, prometaphase,

metaphase, anaphase, telophase & cytokinesis), which are characterised by the

widespread reorganization of subcellular architecture. For example, in prophase,

duplicated centrosomes separate to form the poles of the mitotic spindle. Centrosome

separation is dependent on the activities of several kinases, including Cdk1 and Plk1

(Smith et al. 2011), and on the microtubule motor protein Eg5 (Sawin et al. 1992).

Improperly timed centrosome separation can lead to chromosomal instability, as shown

in cyclin B2-overexpressing MEFs (Nam & van Deursen 2014). From prophase to

prometaphase, nuclear envelope breakdown occurs and spindle assembly begins.

During prometaphase, proper kinetochore microtubule attachments form, which

depend on the interaction of each kinetochore on the sister chromatids forming stable,

end on attachments to spindle microtubules. The recruitment of Eg5 to spindle

63 microtubules is promoted by the microtubule-nucleating protein TPX2 (Eckerdt et al.
64 n.d.; Ma et al. 2010; Ma et al. 2011). Indeed, expression of a TPX2 mutant lacking the
65 Eg5-interaction domain leads to defects in spindle assembly and mitotic arrest (Ma et al.
66 2011).

67 Scheduled degradation of proteins is crucial for linking chromosome alignment
68 and segregation (King et al. 1996) and is therefore an important regulatory mechanism
69 for maintaining genome stability during cell division. Indeed, disruption of the
70 scheduled degradation of key proteins, such as cyclins A and B, can lead to nuclear
71 abnormalities, hyperplasia (Bortner & Rosenberg 1995) and chromosomal instability
72 (Nam & van Deursen 2014).

73 A major challenge with the biochemical analysis of mitosis is that each mitotic
74 subphase is exceedingly short, typically lasting only minutes (Sullivan & Morgan 2007),
75 with cell-to-cell variability in dwell times. This has hampered attempts to perform a
76 comprehensive analysis of protein abundance changes during mitotic progression due
77 to the difficulty in obtaining highly synchronous cell populations in the various intra-
78 mitotic stages in sufficient numbers for proteome analysis. Additionally, emerging
79 evidence suggests that methods used to either synchronise, or arrest cells in mitosis,
80 may induce artefacts that are not observed during an unperturbed cell cycle (Ly et al.
81 2015). It has also been shown that long-term spindle assembly checkpoint (SAC)
82 activation can lead to what is termed either mitotic 'exhaustion', or 'collapse', due to
83 sustained degradation in the presence of the active checkpoint (Balachandran et al.
84 2016).

85 Technological advances in mass spectrometry (MS)-based proteomics have
86 enabled the large-scale detection and quantitation of proteins, including measurement
87 of properties such as absolute abundances and subcellular localization (Larance &

88 Lamond 2015). However, proteome measurements on either cultured cells, or tissues,
89 reflect average values across a cell population and detailed information on biochemical
90 state heterogeneity is obscured. A powerful approach for separating cellular
91 subpopulations involves immunostaining combined with Fluorescence Activated Cell
92 Sorting (FACS). CyTOF is one example combining the single cell separation power of
93 flow cytometry with accurate mass measurement and quantitation by mass
94 spectrometry (Bendall et al. 2011). In CyTOF, immunological reagents are conjugated
95 with heavy metal isotopes. Cellular material is then atomized for mass analysis of
96 individual atoms, which report on the abundance of the immunological reagent binding
97 to cells. We note that CyTOF, while significantly increasing the number of protein
98 antigens detected as compared with a fluorescence-based assay, does not achieve the
99 same high depth of proteome coverage, extending to thousands of proteins, that can
100 now be obtained by large-scale, MS-based proteomic methods (Hukelmann et al. 2016).
101 Furthermore, apart from lower proteome coverage, CyTOF also has more limited ability
102 to identify post-translational protein modifications and is a target-focused approach, in
103 contrast with the unbiased analysis provided by MS-based proteomics.

104 Until now, studies combining FACS and MS-based proteomics have mostly
105 involved isolating cell subpopulations based on labeling of cell surface antigens, hence
106 avoiding cell permeabilisation and fixation (Di Palma et al. 2011)(Bonardi et al. 2013).
107 Problems with sample bias and protein losses have been encountered in studies using
108 MS-based proteomic methods when cells are permeabilised and fixed (Toews et al.
109 2008), as required for immunodetection of intracellular antigens. Indeed, to avoid
110 intracellular immunostaining, recent work sought to identify mitosis-specific cell
111 surface markers that can be used with live cells to isolate mitotic cell subpopulations in
112 HeLa cells (Ozlu et al. 2015). However, as far as we are aware, neither fluorescence

113 abundance reporter systems, nor cell surface markers, have been reported to
114 distinguish effectively between mitotic subphases, e.g. prophase, prometaphase,
115 metaphase & anaphase, suitable for discrimination and purification by FACS.

116 Previously, we reported a comprehensive proteomic dataset measuring protein
117 and mRNA abundance variation across interphase (G1, S, and G2&M) of the cell cycle
118 (Ly et al. 2014). To prepare cell cycle enriched cell populations, we used centrifugal
119 elutriation (Banfalvi 2011), a method that minimizes physiological perturbation to cells
120 and thus avoids indirect effects modulating gene expression associated with arrest
121 procedures (Ly et al. 2015). While elutriation was effective for isolating interphase
122 subpopulations from human leukemia cells for proteome analysis, there were
123 limitations in resolution. In particular, mitotic cells are poorly enriched relative to G2
124 cells. In contrast, G2 and mitotic cells can be efficiently distinguished using intracellular
125 immunostaining and flow cytometry (Jacobberger et al. 2008; Pozarowski &
126 Darzynkiewicz 2004).

127 Building on our previous work analysing the cell cycle regulated interphase
128 proteome (Ly et al. 2014; Ly et al. 2015), we present here a workflow for performing
129 *proteomics of intracellular immunolabeled subpopulations of cells* (PRIMMUS). Using
130 PRIMMUS, we perform a proteome-wide analysis of changes in protein abundance and
131 phosphorylation during interphase. Further, we perform the first proteomic
132 characterization of distinct mitotic substages, with high enrichment efficiencies
133 between prophase, prometaphase and anaphase in human NB4 cells. All of these
134 proteomic data are freely available, both as raw MS files via the ProteomeXchange
135 PRIDE repository (<http://www.ebi.ac.uk/pride>, TBA) and as quantified protein-level
136 data, via the Encyclopedia of Proteome Dynamics (www.peptracker.com/EPD), a
137 searchable, online database (Larance et al. 2013).

138 **Results**

139 *Optimization of cell fixation & permeabilisation for proteome analysis*

140 We identified three steps in intracellular immunostaining procedures that have
141 the potential to significantly impact peptide identification by MS-based proteomics: (1)
142 irreversibility and/or chemical modifications associated with cell fixation, (2) loss of
143 soluble proteins during permeabilisation and (3) interference from antibody-derived
144 peptides (Fig. 1A). Therefore, a series of experiments were performed to compare
145 alternative fixation and permeabilisation parameters with respect to these effects.

146 We chose to fix cells with formaldehyde (FA), which has been used extensively
147 for other MS applications, such as protein-protein crosslinking (Larance et al. 2016) and
148 crosslinked immunoprecipitations (Mohammed et al. 2016; Klockenbusch & Kast 2010).
149 FA forms reversible crosslinks that can be broken efficiently at high temperatures.
150 However, prior work on model peptides shows that high FA concentrations can produce
151 irreversible chemical modifications that compromise identification by MS (Toews et al.
152 2008)(Sutherland et al. 2008). FA concentrations and fixation times vary significantly
153 between common immunostaining protocols (Hutten et al. 2014). Therefore, we tested
154 a range of FA concentrations in human myeloid leukemia NB4 cells, employing SDS-
155 PAGE, immunoblotting and total protein gel stains to assay for crosslinking efficiency
156 (Fig. 1B). This identified 0.5% as the minimum concentration of FA that fixes cells and
157 produces high-MW PAGE-impermeable crosslinked products. As shown by
158 immunoblotting, crosslinking results in α tubulin migrating at increasingly higher MW
159 bands in a FA-dependent manner, with no monomer remaining at 4% FA (Fig. 1FS1A). A
160 similar FA-dependent shift is observed for histone H3 (Fig. 1FS1B). These data show
161 that while 0.1% FA is sufficient to observe crosslinked proteins, 4% FA is required to

162 crosslink most of the total protein pool. However, high FA concentrations reduce the
163 efficiency of reverse-crosslinking, as discussed below.

164 To test the efficiency of reverse-crosslinking, FA-fixed lysates were heated at 95
165 °C for 30 min, electrophoresed under reducing conditions and total protein visualized
166 by SyproRuby staining (Fig. 1C). The 17-kD band that was lost in a FA concentration-
167 dependent manner (Fig. 1B, arrow), was recovered upon crosslink reversal (Fig. 1C,
168 arrow). However, high MW bands, indicated by an asterisk, are still observed at 4% FA
169 after heating. Quantitation of the summed intensity within the top third of the gel
170 indicates a ~20% increase in intensity in 4% FA, compared with 0% FA, likely due to
171 irreversibly crosslinked high MW protein-protein complexes. Consistent with the Sypro
172 Ruby stain data, immunoblots show that the pools of crosslinked α -tubulin and histone
173 H3 multimers, produced by treatment of cells with 4% FA, are heat stable (Fig. 1FS
174 1C&D).

175 Protein-DNA crosslinks created by FA can affect the accuracy of measuring DNA
176 content by flow cytometry and thus may decrease the resolution with which cell cycle
177 phases can be separated. We measured the DNA content of cells fixed with the indicated
178 FA concentrations, permeabilised with 70% ethanol and stained with either propidium
179 iodide (PI, left), or with 4',6-diamidino-2-phenylindole (DAPI, right), (Fig. 1FS2).
180 Hoechst-33342 gave inferior results (data not shown). PI staining of cells treated with
181 0% FA produces low coefficient-of-variation (CV) values, e.g. 5.6% for G1, which
182 increase in a FA dose-dependent manner. Peaks for 2N and 4N DNA content (i.e., G1 and
183 G2&M phases), coalesce at 1% and higher concentrations of FA. DAPI showed slightly
184 higher starting CV values (7.3% for G1), but, unlike PI, was minimally affected by FA
185 concentration. We conclude that, with these fixation conditions, 0.5% FA is the
186 maximum for optimum use with PI, while 4% FA can be used with DAPI. In experiments

187 where quantitation of DNA content by PI is not required to isolate a cell subpopulation
188 of choice, then up to 2% FA can be used in combination with the intracellular staining
189 protocol, with minimal protein loss (Fig. 1C).

190 Quantitative comparisons of protein levels using stable isotope labeling by
191 amino acids in cell culture (SILAC)(Ong et al. 2002), are internally controlled, thereby
192 minimizing the effect of technical variation after mixing on the accuracy of quantitation.
193 We therefore used SILAC to evaluate how alternative permeabilisation reagents affect
194 proteome recovery. For compatibility with both PI and DAPI staining and efficient
195 crosslink reversal, cells were fixed with 0.5% FA. Three protocols were compared (Fig.
196 1D): (i) cells were fixed and permeabilised with 0.5% Triton X-100, (ii) cells were fixed
197 and permeabilised with 90% methanol and (iii) cells were lysed without fixation and
198 permeabilisation. Cells were then mixed pairwise 1:1 by cell count and processed for
199 'single shot' MS analyses (Supplementary Table 1).

200 The log₂-transformed normalized ratios were analysed in scatter plots (Figs. 1E-
201 G). In Fig. 1E, the position of each point relative to the x-axis represents the ratio
202 between the abundance of a single protein measured in cells permeabilised with Triton
203 X-100, (method i), and the same protein in cells processed by lysis only (method iii).
204 Points are offset on the y-axis to minimise overplotting. Proteins detected equally in
205 each method will show a ratio of 1, while irreversible FA-induced protein modifications
206 and/or losses due to permeabilisation will cause lowered ratios. Known FA-induced
207 modifications, such as methylol and Schiff base intermediates (producing +30 and +12
208 mass shifts, respectively), were identified after adding these modifications to the search
209 database. However, only a small number of peptides (<1%) were found to be modified
210 (data not shown). Proteins annotated with the subcellular localization GO terms,
211 'membrane' and/or 'mitochondrial', are shown in purple.

212 Triton X-100 is widely used in protocols for cell permeabilisation when
213 immunostaining intracellular antigens (Hutten et al. 2014). However, we observe that
214 many proteins are depleted in Triton-X100-treated cells (Fig. 1E). Proteins showing
215 lower ratios after Triton-X100 permeabilisation are enriched for ‘mitochondrial’ and/or
216 ‘membrane’ GO terms (Fisher’s exact test for enrichment: $p < 1 \times 10^{-25}$ for mitochondria
217 and $p < 1 \times 10^{-20}$ for membrane GO annotations). In contrast, a comparison of methanol
218 permeabilisation with direct lysis shows that most proteins vary <2-fold (Fig. 1F).
219 However, the levels of some proteins were reduced following methanol treatment. To
220 investigate whether this was stochastic, we compared two technical replicates of
221 methanol-permeabilised cells using SILAC (Fig. 1G). The low variance between the
222 replicates indicates that the effects of methanol permeabilisation on protein extraction
223 and measurement efficiencies are systematic and reproducible. However, GO annotation
224 analysis shows no significant enrichment for the proteins with decreased abundance
225 after methanol permeabilisation (Fig. 1F). The reason for the selective protein loss is
226 therefore not clear but is unlikely to significantly bias downstream proteome analyses
227 between samples that have been similarly methanol-treated. In summary, we conclude
228 that methanol is preferred over Triton-X100 as a permeabilisation reagent for
229 downstream proteome analysis under these fixation conditions.

230 These data identify a protocol for immunostaining intracellular antigens that is
231 compatible with efficient downstream MS-based peptide ID and quantitation and that
232 minimizes loss of protein identifications. While the fixation and permeabilisation steps
233 slightly reduce the overall peptide signal (Fig. 1F), these decreases are reproducible and
234 can be accounted for in performing relative comparisons of protein abundance (Fig. 1G).
235 We term the resulting methodology using this optimized protocol, ‘PRIMMUS’
236 (*Proteomics of intracellular immunostained cell subpopulations*).

237 *PRIMMUS analysis of protein accumulation across the cell division cycle*

238 The PRIMMUS methodology is well-suited for transforming end-point
239 immunostaining flow cytometry assays for cell cycle analysis into a preparative
240 procedure for global proteome characterisation. For example, G1, S and G2&M cell
241 populations can be distinguished by DNA content alone using flow cytometry. As G2 and
242 M phase cells have identical DNA content and similar size distributions, an additional
243 parameter is required to separate these phases. H3S10ph, which accompanies mitotic
244 chromatin condensation (Hendzel et al. 1997), is a specific marker for mitotic cells in
245 many cell types and across many phyla (Hans & Dimitrov 2001). H3S10ph staining is
246 often used as a proxy for mitotic index, particularly in flow cytometry assays (Juan et al.
247 1998), because only mitotic cells are H3S10ph positive. The specificity of the anti-
248 H3S10ph antibody for mitotic cells also aids an evaluation of the potential effect of
249 antibody IgG peptides on peptide identification.

250 SILAC-labeled cells were fixed, permeabilised, immunostained and sorted into
251 four subpopulations (i.e., G1, S, G2, and M), based on both DNA content and H3S10ph
252 staining, then processed for MS analysis, as illustrated in Fig. 2A. Four subpopulations
253 are discernable in a representative pseudocolour scatter plot of the flow cytometric
254 analysis, showing H3S10ph staining (y-axis), versus DNA content (x-axis) (Fig. 2B). Cells
255 were sorted into G1, S, G2 and M fractions using the sorting 'gates' indicated (Fig. 2B,
256 black boxes). The purities of G2 and M fractions were validated by co-immunostaining
257 fractionated cells with anti-alpha tubulin antibodies and analysis by
258 immunofluorescence (Fig. 2C). This showed that none of the cells in the G2 fraction
259 were mitotic and >96% of cells in the M fraction were mitotic, as evaluated by
260 chromatin condensation and microtubule organization (Fig. 2D).

261 The variation in relative protein abundance among the four sorted
262 subpopulations of cells was determined using SILAC quantitation in single shot MS
263 analyses (Fig. 2E). Flow sorted “heavy” cell populations were mixed with equal numbers
264 of asynchronous “light” cells, with the signal from the “light” cells used as an internal
265 standard to compare the four sorted populations (Fig. 2E). Four biological replicates
266 were performed to evaluate biological variance.

267 In total, 32,066 peptides were identified from the four replicate experiments
268 (raw data available at the ProteomeXchange Consortium, identifier TBA). These peptide
269 measurements enabled quantitation of 3,696 proteins, of which 3,162 have at least two
270 supporting peptides per protein (Supplementary Table 2). A comparable number of
271 proteins were identified when the identical single shot MS analysis was performed on a
272 standard complex peptide mixture prepared from directly lysed human NB4 cells (Ly et
273 al. 2014). All cells in the asynchronous population are exposed to the H3S10ph
274 antibody, yet only M-phase cells carry the antigen and are immunostained. Thus, the
275 recovered M phase fractions will have IgG proteins that will be largely absent in the
276 other fractions. Peptide ID and quantitation rates are similar across sorted populations
277 (Fig. 1F), indicating that antibody-derived peptides present in the cell extracts from the
278 M-phase fraction do not significantly hinder the MS-based peptide ID rate.

279 Because the SILAC mixing was performed using equal numbers of cells from each
280 population, rather than equal amounts of protein, as determined either by mass, or
281 concentration, the ratios measured here reflect the variation in average protein
282 abundance at the respective G1, S, G2 and M phases during an unperturbed cell division
283 cycle. Fig. 3A shows a modified violin plot (here, called a ‘neeps’ plot) of \log_2 ratios
284 versus sort population (G1, S, G2 and M). The width of each ‘neep’ is proportional to the
285 number of proteins. Black lines mark quartiles and shading indicates interquartile

286 ranges. Compared with the internal standard (asynchronous cells), G1 cells have a
287 median ratio of ~ 0.8 and mitotic cells a median ratio of ~ 1.3 . Thus, an average M phase
288 cell contains $\sim 1.6x$ the number of protein molecules present in an average G1 cell. This
289 value is less than 2 (the approximate ratio theoretically expected between a newly
290 divided cell and a mitotic cell), because the 'average' G1 cell has already spent several
291 hours in G1 phase, during which time new protein synthesis has commenced.

292 Using the average doubling time for NB4 cells (24 hours) and the frequency of
293 cells in each cell cycle phase, as measured by flow cytometry, we use ergodic analysis
294 (Pozarowski & Darzynkiewicz 2004; Wheeler 2015; Kafri et al. 2013) to estimate the
295 average time post-division for each subset of cells and express them as a fraction of the
296 total cell division time, i.e. $t = 0$ (newly divided), $t = 0.21$ (G1), $t = 0.65$ (S), $t = 0.92$ (G2), t
297 $= 0.98$ (M) and $t = 1.0$ (cell division). This representation of the relative cell cycle
298 division time (Fig. 3B, inset), allows protein abundance data to be plotted on a
299 numerical time axis and provides a quantitative measurement of protein accumulation
300 across the cell cycle.

301 Global changes in relative protein abundance at different cell cycle stages were
302 estimated by taking the mean \log_2 SILAC measurement across all proteins. Mean protein
303 measurements were calculated for each cell cycle phase, normalized to G1 and plotted
304 as a function of cell division time, with error bars indicating the standard error of the
305 mean (Fig. 3B). Bulk protein abundance accumulation across the cell cycle follows an
306 exponential growth curve ($r^2 = 0.99$) (Fig. 3B). Bulk protein abundance is measured to
307 increase ~ 1.9 -fold between a newly divided cell and a cell about to enter the next
308 mitosis phase. These findings are consistent with results from experiments performed
309 decades ago, using radioactive pulse-chase experiments to analyse bulk protein
310 accumulation (Scharff & Robbins 1965)(Rønning et al. 1979). However, using

311 PRIMMUS, the relative protein accumulation across the cell cycle is measured here not
312 on bulk protein alone, but rather on a per-protein basis for thousands of individual
313 proteins.

314 We exploited the per-protein resolution of our data to examine whether different
315 protein classes accumulate at different rates during the cell cycle. Fig. 3C shows a
316 heatmap summarising an analysis of the mean normalized ratio for proteins with GO
317 annotations for major cellular processes, i.e., transcription, mRNA splicing, translation,
318 DNA replication and mitosis (Fig. 3C). As expected, proteins involved in DNA replication
319 increase more on average during S phase than proteins involved in basal gene
320 expression (transcription, mRNA splicing, translation).

321 We show individual profiles for selected proteins in Fig. 3D. Aurora kinase A,
322 which regulates spindle assembly in mitosis (Floyd et al. 2008), increases in abundance
323 by more than 8-fold between G1 and M phase (Fig. 3D). Core histones, however, show a
324 profile that resembles bulk protein accumulation and approximately double in
325 abundance across the cell cycle, consistent with the parallel doubling in DNA content.
326 However, while bulk protein continues to accumulate between G2 and M (Fig. 3D),
327 histone abundance remains relatively flat, consistent with histone protein synthesis
328 being markedly down-regulated once S phase is completed (Fig. 3D). Interestingly, in
329 contrast with bulk cellular proteins, we note that proteins involved in stress responses
330 and/or apoptosis, such as p53, NKAP (a member of the NF-kappa B pathway) and the
331 apoptotic regulators BAX and BID, remain relatively constant on a per-cell basis across
332 these four cell subpopulations.

333 Using FACS, each cell cycle phase is enriched with higher purity as compared
334 with centrifugal elutriation. We therefore analysed whether this results in the PRIMMUS
335 method providing increased sensitivity for detecting relative changes in protein

336 abundance between cell cycle phases. Fig. 3E shows a comparison between datasets
337 obtained using either PRIMMUS (red circles), or elutriation (blue triangles), for 14
338 proteins that all peak in abundance in G2/M relative to G1 phases (i.e., CDC20, AURKA,
339 KIFC1, CCNB1, ANLN, HMMR, KIF20A, AURKB, CCNB2, RRM2, PLK1, RACGAP1, CENPF &
340 PRC1). All these 14 proteins show higher ratios in the PRIMMUS dataset. We conclude
341 that the higher enrichment purities for cell subsets obtained by FACS results in
342 PRIMMUS providing a sensitivity advantage over centrifugal elutriation.

343 *PRIMMUS analysis of protein phosphorylation across interphase and mitosis*

344 We next investigated protein phosphorylation changes during interphase and
345 mitosis using PRIMMUS. Using the identical sort strategy as above, we separated
346 asynchronous NB4 cells into G1, S, G2 and M phase fractions by FACS (Fig. 4A). The
347 experiment was performed in biological duplicate. The cell fractions were then
348 processed for phosphopeptide analysis and TMT-based quantitation (8-plex, 2
349 biological replicates x 4 cell cycle phase fractions). Enriched phosphopeptides with no
350 further peptide fractionation were detected and quantitated using a single shot LC-
351 MS/MS analysis. In total, 4,500 phosphorylation sites were identified on 1,558 proteins.
352 Most phosphorylation sites were phosphoserines (83.2%), with smaller frequencies for
353 phosphothreonines (15.8%) and phosphotyrosine (1.0%) (Fig. 4B). Over 60% of the
354 phosphorylation sites matched the proline-directed kinase motif (S/T followed by a
355 proline (Fig. 4C). CDKs are one of several kinases, e.g. MAP kinases, which can
356 phosphorylate the [S/T]P motif (as reviewed in (Amanchy et al. 2007)). The
357 phosphoproteins detected are enriched in proteins with functions in cell division and
358 DNA repair/stress response, in addition to 'housekeeping' proteins involved in gene
359 expression (Fig. 4D). The phosphorylation site abundance profiles for the duplicate
360 measurements were similar (Fig. 4E). As discussed in more detail below, many of the

361 extreme differences in phosphorylation are observed in the mitotic fraction. Pearson
362 correlations calculated for individual phosphorylation sites showed high correlation
363 (Fig. 4F). The maximum fold changes measured for individual phosphorylation sites
364 were also highly correlated between the two replicates, showing that the quantitation
365 was reproducible (Fig. 4G).

366 The identified phosphorylation sites were then clustered using k-means into six
367 groups (Fig. 5A). Cluster 1 contains phosphorylation sites that rise significantly during
368 mitosis. Interestingly, many of these sites also show an increase in the G2 fraction (Fig.
369 5A, arrow). Clusters that peak in mitosis (1, 2, 3 and 5) represent 34% of the
370 phosphorylations quantitated (Fig. 5B). Interestingly, this number is significantly
371 smaller than reported previously in a study measuring phosphorylation dynamics in
372 HeLa cells synchronized using nocodazole arrest and arrest-release protocols (Olsen et
373 al. 2010). A comparison of the ratios measured in the PRIMMUS dataset with this
374 previous analysis shows significant differences. We note that phosphorylation sites
375 specifically upregulated in this PRIMMUS dataset are on proteins that are enriched for
376 the gene ontology annotations 'cell cycle' and 'mitosis' (Fig. 5C, purple). In contrast,
377 phosphorylation sites specifically upregulated in the previous HeLa cell arrest-release
378 dataset (which are not changing in this PRIMMUS dataset), are instead on proteins
379 showing significant enrichment for the gene ontology annotation 'RNA splicing function'
380 and show no enrichment for either 'mitosis', or 'cell cycle' (Fig. 5C, cyan). These
381 differential enrichments in specific cellular functions for the proteins identified with
382 changing levels of phosphorylation across the cell cycle suggest underlying
383 physiological differences between the cells used in these respective studies (see also
384 Discussion).

385 *Identification of a set of 'early rising' phosphorylation sites*

386 While most of the significantly changing phosphorylation sites peak in mitosis, a
387 subset, consisting of 115 sites, also show significantly increased phosphorylation in the
388 G2 phase enriched fraction. We have termed these 115 phosphorylation sites, ‘early
389 risers’. The high enrichment efficiency of FACS (c.f. Fig. 2C) renders it very unlikely that
390 the increased G2 ratios measured originate from contamination from H3S10ph-positive
391 mitotic cells in the G2-enriched fraction. Indeed, further analysis shows that early risers
392 share additional functional similarities. Thus, early rising phosphorylation sites are
393 situated on proteins highly enriched in nuclear, nuclear envelope and chromatin
394 localisations (Fig. 6A). A STRING network analysis identifies several functional
395 categories of early rising proteins, including DNA replication, cytoskeleton remodelers
396 and spindle/kinetochore components, chromatin factors and remodelers, nuclear
397 envelope proteins, transcription factors, nucleolar proteins and mRNA capping proteins.
398 Proteins with the highest ranked ratios are either involved in DNA replication, or
399 associated with the nuclear envelope (Supplementary Table 2). Motif analysis shows
400 that early risers are enriched in the optimal CDK consensus motif of a serine/threonine
401 followed by a proline and a downstream basic residue (Figure 6C). Consistent with a
402 high CDK phosphorylation propensity, early risers on average have higher
403 phosphorylation ratios during M-phase compared to ‘late risers’, (i.e. late risers being
404 phosphorylation sites that peak in mitosis and do not increase in G2).

405 One of the early risers identified was on the protein TPX2. Two TPX2
406 phosphorylation sites are quantitated in this dataset, i.e., S185 and S738. Both sites have
407 surrounding sequences matching the consensus CDK phosphorylation motif (SPEK and
408 SPK, respectively) and show increased phosphorylation in the G2-phase enriched
409 fraction, compared with the total levels of unmodified TPX2 protein. However, TPX2
410 S738 is an early riser site that is phosphorylated to a greater extent in the G2 phase

411 fraction and this difference is further increased in the M-phase fraction. We therefore
412 decided to explore whether there was any functional relevance for phosphorylation of
413 TPX2 at S738 in mammalian cells by analysis of phosphodeficient and phosphomimetic
414 mutants.

415 *Expression of S738A TPX2 mutant fails to rescue TPX2-depleted cells*

416 TPX2 is known to have several functions during mitosis (Neumayer et al. 2014).
417 The N-terminal domain has been shown to be important for interacting with Aurora A
418 kinase (Bayliss et al. 2003) and this interaction facilitates microtubule nucleation at
419 chromosomes (as reviewed in (Gruss & Vernos 2004)). The C-terminal domain has been
420 shown to be important for interaction with Eg5. Cells expressing a C-terminal deletion
421 mutant lacking the Eg5-interaction domain (TPX2-710) shows mislocalisation of
422 spindle microtubule-associated Eg5 and disorganized multipolar spindles (Ma et al.
423 2010; Ma et al. 2011). Interestingly, the early rising phosphorylation site on TPX2,
424 serine 738 (S738), is situated in the Eg5-interaction domain.

425 To assess the function of S738 phosphorylation, endogenous TPX2 was depleted
426 in porcine LLC-Pk1 cells using siRNA and ectopic, GFP-tagged TPX2 was expressed from
427 a rescue construct, comparing the phenotypes of either the wild-type (WT) sequence, a
428 TPX2 phosphomimetic (S738D) mutant, or a TPX2 phosphodeficient (S738A) mutant.
429 Consistent with previous observations (Ma et al. 2011), depletion of TPX2 without
430 rescue leads to an increase in short, collapsed spindles (Fig. 7A, right). Replacement
431 with GFP-TPX2 WT increases the frequency of 'normal' bipolar spindles (Fig. 7A & 7B
432 top). Replacement expression of the phosphomimetic TPX2 S738D mutant also rescues
433 the spindle defect (Fig. 7A & 7B bottom), in a manner similar to replacement expression
434 of TPX2 WT. In contrast, expression of the phosphodeficient TPX2 S738A mutant
435 results in an increase in multipolar spindles (Fig. 7A & 7B middle), a spindle defect

436 similarly observed in cells expressing TPX2-710, a mutant missing the C-terminal Eg5-
437 interaction domain (Ma et al. 2011).

438 Another closely related phenotype associated with replacement of endogenous
439 TPX2 with TPX2-710 is that few, if any, kinetochore fibres are cold stable, indicative of
440 either weak, or improper, kinetochore-microtubule interactions (Ma et al. 2011). We
441 investigated whether a similar phenotype is observed with the TPX2 phosphomutants.
442 Compared to parental cells (Fig. 7C left & Fig. 7D), cells depleted of TPX2 have unstable
443 kinetochore fibres (Fig. 7C right). Cells expressing either WT, or S738D, largely restore
444 kinetochore fibre cold stability (Fig. 7C and D). In contrast, the S738A mutant has an
445 impaired ability to rescue, with many S738A cells showing decreased kinetochore fibre
446 stability. Taken together, we conclude from these data that phosphorylation of TPX2 at
447 S738 is important for its mitotic functions.

448 Because phosphorylation of TPX2 at S738 is observed to be increased in the G2-
449 phase fraction, we next investigated whether TPX2 S738 phosphorylation has a function
450 in earlier mitotic events. One of the earliest events of mitosis is centrosome separation,
451 which occurs prior to nuclear envelope breakdown. Plk1 and CDK activities promote
452 Eg5-driven centrosome separation during late G2 and prophase (Smith et al. 2011). WT
453 TPX2, which is nuclear in interphase (Trieselmann 2003), partially localises to
454 centrosomes and microtubules in prophase (Ma et al. 2011). To assess whether TPX2
455 phosphorylation may play a role in prophase centrosome dynamics, we measured
456 centrosome separation normalized to nuclear area (Fig. 8A) at nuclear envelope
457 breakdown in cells overexpressing either WT, S738D, or S738A TPX2 (Fig. 8 B & C).
458 Interestingly, overexpression of the TPX2 S738A mutant significantly decreases
459 centrosome separation distance, compared either to parental cells, or to cells
460 overexpressing either WT, or S738D TPX2 (Fig. 8B). In addition to the centrosome

461 separation defect, spindle phenotypes manifest after nuclear envelope breakdown in
462 cells overexpressing the TPX2 S738A mutant, as compared to cells overexpressing
463 either TPX2 WT, or the S738D mutant (Fig. 8D & E). Cells overexpressing the TPX2
464 S738A mutant notably show a monopolar spindle phenotype (Fig. 8D bottom). The
465 phenotype penetrance, i.e. the ratio of cells showing monopole vs. bipole spindles,
466 increases with GFP fluorescence bin (Fig. 8F), suggesting that the phenotype is
467 associated with high levels of expression of the TPX2 S738A mutant protein.

468 In summary, we conclude that high levels of a TPX2 mutant that cannot be
469 phosphorylated on residue 738 significantly impairs centrosome separation, an early
470 mitotic event.

471 *PRIMMUS analysis of protein abundance variation during mitosis*

472 We next used the PRIMMUS method to perform a proteomic analysis of protein
473 abundance variation across four temporally distinct stages of mitosis, reflecting
474 prophase, prometaphase (1 & 2, see below) and anaphase. We aimed to screen for
475 proteins that show abundance patterns resembling cyclins A and B, which could reveal
476 novel targets whose degradation is also regulated during mitosis. We chose H3S28ph
477 and cyclin A (CycA), as two markers with which to distinguish different mitotic
478 subphases. Like H3S10ph, the H3S28ph signal is associated with chromatin
479 condensation (as reviewed in (Hans & Dimitrov 2001)). During mitosis, cells undergo
480 reversible condensation of chromatin, with highest levels of compaction observed
481 during prometaphase and metaphase (Hans & Dimitrov 2001). Thus, cells showing the
482 highest levels of H3S28ph signal (H3S28ph-high), represent prometaphase and
483 metaphase cells, while cells showing intermediate levels of H3S28ph signal (H3S28ph-
484 mid), are in early (prophase) and late (anaphase and telophase), stages of mitosis,
485 respectively. Meanwhile, CycA is targeted for degradation by the APC/C during

486 prometaphase in a SAC-independent manner (Elzen & Pines 2001). Thus, comparing
487 either the presence, or absence, of CycA provides a means for distinguishing between
488 'early' (prometaphase and before) vs. 'late' (prometaphase and after) mitotic cells,
489 respectively. Consistent with this, flow cytometry analysis of cells co-immunostained for
490 H3S28ph and CycA show four subpopulations (labelled P1 – P4), which are H3S28ph
491 positive (Fig. 9A).

492 The four subpopulations described above were isolated by FACS and analysed by
493 immunofluorescence microscopy (representative images are shown in Fig. 9A, right).
494 The frequency of interphase, prophase, prometaphase, anaphase and telophase cells
495 were each measured, with at least 100 cells counted for each subpopulation (Fig. 9B).
496 This confirms that high enrichment efficiencies were obtained for prophase,
497 prometaphase and anaphase, respectively. Telophase and cytokinesis cells were not
498 observed in these subpopulations. We note that the gating strategy employed, which
499 removes potential doublets from the analysis, biases against these cells (unpublished
500 observations). Fig. 9C shows a representative image of the P4 subpopulation, showing
501 high enrichment of anaphase cells. Based on these high enrichment efficiencies, we have
502 relabeled these populations according to the major enriched phase represented, i.e.,
503 prophase (Pro), prometaphase 1 (PM1), prometaphase 2 (PM2) and anaphase (Ana),
504 respectively.

505 The FACS protocol was repeated, using three separate asynchronous cell
506 populations cultured and harvested on different days. Two of these populations were
507 metabolically-labelled with stable isotope labelled amino acids for SILAC-based relative
508 quantitation. These populations were sorted into the four subpopulations, P1 – P4, as
509 described above. A third population was cultured using regular culture media
510 containing non-dialysed bovine serum. For this third experiment, two other

511 subpopulations were collected, i.e., G2 cells (i.e., 4N DNA content and pH3 negative
512 cells) and M-phase cells (4N DNA content and pH3 positive cells), in addition to the P1 –
513 P4 populations. Relative quantitation was performed using 6-plex peptide TMT labeling
514 (Thompson et al. 2003). To maximize peptide recovery for MS analysis, the SP3
515 paramagnetic bead cleanup method was used (Hughes et al. 2014). SILAC samples were
516 analysed using a Q-Exactive Plus, as previously described (Endo et al. 2017). TMT
517 samples were analysed using a Fusion Tribrid instrument, using synchronous precursor
518 selection (SPS) (McAlister et al. 2014) to minimize ratio compression. Thus, two
519 distinct relative quantitation strategies were employed to reduce the likelihood of any
520 potential artefacts from a single quantitation strategy to systematically bias the dataset.

521 Quantitative data for >8,700 proteins were obtained in the combined dataset
522 across three biological replicates. 5,205 proteins (60%) were detected in both the TMT
523 and SILAC datasets. To identify proteins whose abundance changed significantly,
524 protein profiles were calculated based on the mean of the three biological replicates and
525 ratios calculated, relative to prophase levels. Proteins showing missing values in any of
526 the four mitotic subpopulations were discarded, leaving 5,340 proteins. A maximum
527 fold change was calculated and cutoffs were established using Z-scores (~1.8-fold at
528 95% confidence), which identified 235 proteins meeting this cutoff. Positive correlation
529 between any two biological replicates was used as a second criterion for significance,
530 with 136 proteins meeting these stringent criteria (Fig. 9E). Several proteins were
531 excluded from the analysis due to missing values, which is a known technical issue with
532 data-dependent acquisition. However, an alternative, non-mutually exclusive
533 explanation, is the lack of detection reflects that the levels of these proteins fall below
534 the detection limit due to physiological down-regulation. We reasoned that the latter
535 explanation is more likely when proteins show missing values reproducibly in a single

536 fraction. Two proteins met this criterion and were added to the candidate list
537 (Supplementary Table X), which now totals 138 proteins. However, these two proteins
538 were excluded in further clustering analysis due to missing values being incompatible
539 with the standard k-means clustering algorithm. The vast majority of proteins (n =
540 5,202, ~98.5%), showed no significant change (Fig. 9E).

541 The mean profiles for the 136 proteins showing the most significantly changing
542 abundance levels were clustered using k-means, with the number of initial clusters (12)
543 determined using a within-cluster sum-of-squares analysis. Within this dataset we were
544 interested in identifying candidates for targeted protein degradation during mitosis. We
545 therefore focused on those clusters where a decrease in protein abundance was evident.
546 These were manually agglomerated into three clusters, based on the phase in which the
547 decrease is observed (Fig. 9F). Most of these proteins (79%), show a decrease in
548 abundance coincident with the CycA+ prometaphase subpopulation (PM1), with fewer
549 proteins (16%), decreasing in anaphase and fewer still (5%) decreasing in the CycA-
550 prometaphase subpopulation (PM2).

551 We next examined the mean protein abundance profiles for cyclins A and B (Fig.
552 10A, s.d. shown as a gray ribbon). As expected from the flow cytometry analysis and the
553 sorting strategy employed, cyclin A2 shows high levels in Pro and PM1 and a marked
554 decrease in PM2 and Ana. Two isoforms of cyclin B are detected (B1 and B2). The
555 abundances of both isoforms remain relatively constant between Pro, PM1 and PM2 and
556 decrease in Ana to 25-35% of prophase levels. These data are consistent with the
557 targeting of cyclin B for degradation by the APC/C at the metaphase to anaphase
558 transition. In contrast, the abundance of GAPDH, a protein that is not expected to be
559 targeted for degradation during mitosis, is unchanged between these subpopulations.
560 *RRM2 is degraded during prometaphase via a MLN-4924-sensitive proteasomal pathway*

561 We were interested in examining other proteins that co-clustered with the cyclin
562 proteins. In the literature, there are few examples of substrates targeted for degradation
563 during prometaphase, as compared with anaphase. We are aware of only two proteins,
564 cyclin A2 and Nek2, for which there is significant evidence in the literature for targeted
565 degradation during prometaphase (van Zon & Wolthuis 2010). Our data show 3
566 additional proteins clustering together with cyclin A2, i.e., ATAD2, GMNN and RRM2.
567 Inspection of the protein abundance profiles show that while GMNN levels decrease
568 during prometaphase to ~60% of prophase levels, a second major decrease in GMNN
569 abundance occurs during anaphase, where its levels drop to ~20%. ATAD2, a protein
570 involved in transcriptional co-activation of cell cycle genes, such as c-myc, cyclin D1 and
571 E2F1, shows ~50% reduction during prometaphase. ATAD2 contains a conserved,
572 canonical D-box motif situated in a disordered linker region between a predicted DNA-
573 binding bromo- domain and a second globular domain. ATAD2 was also recently shown
574 to be cell cycle regulated via co-immunostaining of FUCCI-expressing cells with a rabbit
575 polyclonal antibody recognizing ATAD2 (Human Protein Atlas, www.proteinatlas.org).

576 We investigated further the observed degradation of RRM2. RRM2 is an essential
577 (Wang et al. 2015), cell cycle regulated subunit of ribonucleotide reductase that
578 regulates the cellular deoxynucleotide pool (Nordlund & Reichard 2006). Properly
579 timed degradation of RRM2 has been suggested to be important, because disrupting the
580 normal degradation timing for RRM2 leads to genomic instability (D'Angiolella et al.
581 2012). RRM2 has been shown to be targeted for degradation by the APC/C-Cdh1
582 (Chabes et al. 2003) and Cyclin F/SCF (D'Angiolella et al. 2012) complexes during
583 anaphase and in G1 and G2, respectively. Therefore, we were surprised to observe
584 significant decreases in RRM2 abundance specifically during prometaphase, coincident
585 with degradation of cyclin A2 (Fig. 10B).

586 A rabbit polyclonal antibody raised against RRM2 was validated by siRNA
587 depletion (Fig. 10 Fig. Suppl. 1) and used to measure the levels of RRM2 across the cell
588 cycle in NB4 cells. Consistent with its degradation by APC/C-Cdh1, flow cytometry
589 analysis of RRM2 levels and DNA content show that RRM2 levels are low during G1
590 phase and increase significantly during S-phase, reaching a peak in G2&M (Fig. 10C).
591 Interestingly, this analysis shows no significant decrease in RRM2 levels in G2, as was
592 previously reported in HeLa cells (D'Angiolella et al. 2012). Co-immunostaining cells to
593 detect both cyclin A and H3S28ph enables a flow cytometry-based comparison of RRM2
594 levels, using the same gating strategy as the MS-based analysis used to define
595 subpopulations. A separate control sample, using an antibody recognizing alpha tubulin,
596 was included as a negative control. Fig. 10D shows the fluorescence signal distributions
597 for two subpopulations marked by H3S28ph and CycA staining: i.e., CycA+
598 prometaphase (PM1) versus CycA- prometaphase (PM2) cells. Comparing protein levels
599 in the respective PM1 vs PM2 subpopulations, alpha tubulin shows no change, as
600 expected (Fig. 10D, left). In contrast, the level of RRM2 in PM2 is markedly decreased, as
601 compared with PM1, consistent with the MS-based quantitation (Fig. 10D, right).

602 We next explored potential mechanisms leading to targeted degradation of
603 RRM2. Like CycA, the prometaphase decrease in RRM2 levels occurs in the presence of
604 an active spindle assembly checkpoint (SAC) (Fig. 10E). Mitotic degradation of RRM2 is
605 sensitive to 4 hrs of MG-132 treatment, suggesting that the degradation occurs via the
606 proteasome pathway. Inhibition of APC/C activity, using combined treatment with apcin
607 and proTAME (Sackton et al. 2014), was sufficient to block CycB degradation, but
608 insufficient to stop CycA and RRM2 degradation in NB4 cells. In contrast, treatment with
609 MLN-4924 (Soucy et al. 2009), an inhibitor of NEDDylation and cullin ring ligases
610 (CRLs), completely blocks the decrease of RRM2 levels in prometaphase and leads to

611 levels either similar, or even slightly higher, than observed in control cells (Fig. 10F). As
612 expected, the decrease in CycA in prometaphase is largely unaffected in MLN-4924
613 treated cells (data not shown).

614 We conclude that RRM2 is targeted for proteasomal degradation during
615 prometaphase via a MLN-4924-sensitive pathway, probably involving an SCF complex.
616 As discussed further below, a likely candidate is the cyclin F/SCF complex, as RRM2 has
617 been described previously as a substrate of this E3 ligase (D'Angiolella et al. 2012).

618 To maximize community access to the entire dataset described in this study,
619 including the optimization experiments and the measurements of protein accumulation
620 across the cell cycle, all of the proteomics data are freely available via several outlets,
621 including the Encyclopedia of Proteome Dynamics (<http://www.peptracker.com/epd/>)
622 (Fig. 11). The EPD provides a searchable, open access database containing also
623 proteome measurements from multiple large-scale experiments on human cells and
624 model organisms (Larance et al. 2013). The data are also available at various stages of
625 analysis, including raw MS files and MaxQuant-generated output (ProteomeXchange)
626 and analysed data (Supplementary Tables).

627 **Discussion**

628 A major challenge with the biochemical analysis of mitotic cells is that each sub-
629 phase of mitosis is exceedingly short, lasting only minutes or less (Sullivan & Morgan
630 2007). Additionally, there is significant cellular heterogeneity in phase dwell times.
631 Timing heterogeneity, which can be accounted for in timelapse imaging studies
632 (Akopyan et al. 2014), present major technical challenges to synchronization-based
633 strategies for biochemical analysis. In this study, we characterize the PRIMMUS method,
634 which provides a flexible approach that facilitates quantitative proteomic studies on
635 specific cell subsets isolated by FACS on the basis of staining for *intracellular* antigens.

636 For separation of interphase cells (G1, S, G2), centrifugal elutriation is an alternative to
637 FACS, but provides lower resolution separation, is not applicable to all cell types and
638 does not efficiently separate G2 and M phase cells. We therefore used FACS to produce
639 highly enriched populations of cells at specific cell cycle stages. Cells growing in
640 asynchronous cultures were FACS separated by either, a) DNA content and
641 phosphorylation of histone H3, obtaining high purity populations of G1, S, G2 and M
642 phase cells, or by b) DNA content, phosphorylation of histone H3 and the degradation of
643 CycA, obtaining high purity populations of prophase, prometaphase and anaphase intra-
644 mitotic cells. Using these isolated cell populations, we provide the first specific MS-
645 based proteomic analysis of intra-mitotic phase cells isolated from asynchronously
646 growing cultures.

647 We validated the PRIMMUS method by demonstrating that global MS-based
648 protein identification and quantitation is compatible with the analysis of populations of
649 fixed cells that have been permeabilised, stained to detect *intracellular* antigens and
650 isolated by FACS. While FACS has been used previously in conjunction with RNA-seq to
651 compare mRNA abundances of cell subsets (Hrvatín et al. 2014), this study provides the
652 first example we know of where permeabilised, fixed and intracellular immunostained
653 cells have been FACS sorted and used for quantitative, MS-based proteome analysis. In
654 principle, the PRIMMUS approach can be used to characterize any distinct type of cell
655 subpopulation that can be defined using one or more diagnostic antigens, an abundance
656 differential for a specific epitope, or combination of epitopes, including intracellular and
657 intranuclear antigens. We also show that PRIMMUS enhances the sensitivity of
658 quantitative proteomics technology to detect either changes in abundance, and/or
659 changes in other protein properties, such as post-translational modifications, because it
660 facilitates the analysis of the specific subsets of cells in which the change occurs,

661 without diluting this signal by analyzing mixed populations, including non-responding
662 cells. This is illustrated here by our demonstration of up to a five-fold sensitivity gain in
663 detecting cell cycle regulated protein abundance changes, as judged by comparing data
664 obtained using PRIMMUS with centrifugal elutriation.

665 We have recently shown by proteomic analysis of NB4 cells after arrest at
666 specific cell cycle stages by drug treatments that the stress resulting from drug arrest
667 causes major changes in the proteome distinct from the physiological regulation of
668 protein levels during unperturbed cell cycle progression (Ly et al. 2015). In the
669 PRIMMUS method, fixation by FA captures cells ‘frozen in motion’ and thereby prevents
670 significant perturbation of cellular physiology due to extended sample handling.
671 Consistent with this idea, we previously showed that that the abundance of the
672 apoptosis-associated protein BID is upregulated by the CDK1 inhibitor RO-3306, which
673 arrests cells at the G2 and M border (Ly et al. 2015). In this study, using PRIMMUS, we
674 observe BID levels stay relatively constant across the unperturbed cell cycle, consistent
675 with our results comparing minimally perturbed cells separated by centrifugal
676 elutriation (Ly et al. 2014). While FACS can also be used to sort live cells, thereby
677 avoiding procedures involving fixation and permeabilisation, the process of FACS-based
678 separation of live cells can induce cellular stress and this in turn can rapidly alter the
679 proteome. The proteomes of live cells immediately after FACS may thus be significantly
680 remodeled by activation of cellular stress responses. Furthermore, most live cell
681 strategies require the construction of transformed cell lines expressing one or more
682 fluorescent-tagged fusion proteins. In contrast, the PRIMMUS approach described here
683 avoids any requirement for the use of exogenous, tagged proteins and provides a
684 general strategy that can be applied to both cultured cell lines and primary cells isolated
685 *ex vivo*.

686 We used PRIMMUS, combined with high accuracy cell mixing and quantitative
687 metabolic labeling, to measure and compare the abundances of thousands of individual
688 proteins across an unperturbed cell division cycle, including different substages of
689 mitosis. Our data show that while exponential accumulation is observed for bulk
690 protein, the rate of accumulation of individual proteins can deviate significantly from an
691 exponential growth fit. For example, histones, which constitute ~3-5% of the total
692 protein abundance in NB4 cells (Ly et al. 2014), deviate from bulk protein accumulation
693 by remaining flat between G2 and M, consistent with the synchronization of DNA
694 replication and histone synthesis (Nelson et al. 2002):(Robbins & Borun 1967).
695 Intriguingly, for p53 and some other proteins associated with stress responses and/or
696 apoptosis, protein abundance remains relatively flat across the cell division cycle. Due
697 to cell cycle-dependent increases in cell size and bulk protein abundance, the effective
698 net intracellular concentrations of these proteins must thus decrease as the cell cycle
699 progresses. Any functional consequence of a decrease in their abundance may however
700 be offset if mechanisms exist to create local concentration hotspots at specific
701 subcellular locations.

702 Detailed proteomic analysis of protein abundances across prophase,
703 prometaphase and anaphase cells showed that only ~1.5% of the proteins quantitated
704 significantly decrease in abundance. These proteomic data showed RRM2 levels
705 decreasing during prometaphase. Consistent with this, subsequent flow cytometry
706 analysis showed that RRM2 and CycA levels are correlated during mitosis. The decrease
707 in RRM2 levels was prevented by treatment of cells with either MLN-4924, or MG-132,
708 consistent with the mechanism causing a decrease in RRM2 levels involving a cullin E3
709 ubiquitin ligase and proteasomal degradation. It has been shown that RRM2 is targeted
710 for degradation by Cyclin F/SCF during G2 (D'Angiolella et al. 2012) and several studies

711 have shown co-immunoprecipitation of RRM2 and Cyclin F in asynchronous cell
712 extracts (D'Angiolella et al. 2012; Huttlin et al. n.d.; Hein et al. 2015). It has also been
713 reported that disruption of the Cy motif in RRM2, which is important for recognition by
714 Cyclin F/SCF, stabilizes RRM2 levels and increases DNA pools and genome mutation
715 frequencies (D'Angiolella et al. 2012). It will be interesting in the future to investigate
716 further the timing of RRM2 degradation and its relation to maintaining genome
717 stability.

718 We show that PRIMMUS is compatible also with analysis of cell cycle regulated
719 protein phosphorylation by comparing phosphorylation in G1-, S-, G2- and M-phase
720 enriched fractions purified by FACS. While essentially all significantly changing
721 phosphorylation sites peak during mitosis, we identify a subset of phosphorylation sites
722 that show increased phosphorylation in the G2-enriched fraction, which we call 'early
723 risers'. These early risers share functional similarities, including enrichment in the
724 'classic' CDK substrate phosphorylation motif and localization to chromatin and the
725 nuclear envelope. We suggest that these early rising sites may be the downstream effect
726 of mitotic entry kinase activity, which includes Plk1 and Cdk1 (Smith et al. 2011).
727 Interestingly, the sites that change by the highest amount in G2, besides factors strongly
728 associated with DNA replication, are localized to the nuclear pore and nuclear envelope.
729 Additionally, several sites, such as on lamina-associated polypeptide 2 (LAP2) and
730 NUP153, contain both Plk1 and Cdk substrate sequence motifs (Supplementary Table
731 2). An expanded analysis of phosphorylation during S- and G2-phases will be an
732 important goal of future studies and will help to define the targets of the mitotic entry
733 network in detail. This may provide clues to the sequence of signaling events that
734 precede nuclear envelope breakdown.

735 When the phosphoproteomic dataset from this study was compared with a
736 previously reported atlas of mitotic phosphorylation in human cells derived using
737 nocodazole arrested HeLa cells (Olsen et al. 2010), some phosphorylation sites were
738 identified that changed in one dataset, but not the other. The sites that differed between
739 the two datasets were preferentially on proteins with specific functional GO
740 annotations, including 'cell cycle' and 'mitosis' for phosphorylation sites that are
741 changing exclusively in the mitotic fraction in this PRIMMUS dataset, but instead
742 proteins with phosphorylation sites that are changing exclusively in the mitotic fraction
743 in the previously reported HeLa dataset are enriched for the annotation 'splicing' and
744 not 'cell cycle' or 'mitosis'. Several differences between these studies could explain
745 study-specific phosphorylation changes. For example, cell-type specificity in cell cycle
746 regulated protein phosphorylation, e.g. NB4 cells (this study), as compared with HeLa
747 cells used in the previous study. An alternative, non-mutually exclusive, explanation
748 could be the difference in the methods used for obtaining mitotic cells in the respective
749 studies, i.e. FACS (this study) vs nocodazole-arrest (HeLa dataset (Olsen et al. 2010)).
750 Previous work has shown that cell cycle arrests can induce proteomic changes that are
751 not observed in a minimally perturbed cell cycle (Ly et al. 2015). Further analysis will
752 be required to investigate the basis for the observed study-specific phosphorylation
753 changes.

754 We show that for the TPX2 protein, the phosphorylation increase observed
755 during G2 and mitosis has functional consequences on protein function and proper
756 mitotic progression. Thus, mutation of the early rising phosphorylation site, S738, on
757 TPX2 to a non-phosphorylatable residue (alanine), elicits a significant reduction in
758 centrosome separation and defects in bipolar spindle assembly, when overexpressed.
759 The C-terminal 37 amino acids (including S738) have been shown to be important in

760 recruiting Eg5 to spindle microtubules and modulating Eg5-dependent microtubule
761 gliding activity (Ma et al. 2011). Replacement of endogenous TPX2 with the S738A
762 mutant shows phenotypes intermediate between wild-type and a TPX2 C-terminal
763 deletion mutant lacking the Eg5 interaction domain. Interestingly, both Eg5 and the
764 TPX2 S738A mutant correctly localize to spindle poles and spindle microtubules during
765 mitosis (unpublished observations), suggesting that phosphorylation does not prevent
766 TPX2 from recruiting Eg5 to spindle microtubules. However, the S738A phenotypes
767 suggest that TPX2 S738 phosphorylation plays a key role in affecting the ability of TPX2
768 to modulate Eg5 activity.

769 In addition to the established functions of TPX2 in spindle assembly during
770 prometaphase, evidence in plant cells suggest a second role during early prophase (Vos
771 et al. 2008). In these cells, microinjection of anti-TPX2 antibodies during prophase
772 inhibits nuclear envelope breakdown. In mammalian cells, a subset of TPX2 localises to
773 centrosomes during prophase (Ma et al. 2011). Our present data showing centrosome
774 separation delays with a phosphodeficient TPX2 mutant supports dual roles of TPX2,
775 before and after nuclear envelope breakdown.

776 In addition to PTM analyses, the PRIMMUS workflow can be extended in future
777 by combining it with other complementary approaches to extend the depth of
778 proteomic analysis of the selected cell subpopulations beyond only abundance
779 measurements, e.g. using MS-based techniques for identifying protein interaction
780 partners and protein complexes (Kirkwood et al. 2013)(Kristensen et al. 2012).
781 PRIMMUS is highly complementary to recent studies dissecting, in high resolution, the
782 timing of mitotic kinase activities and quiescence control by automated fluorescence
783 imaging of fixed, immunostained cells (Akopyan et al. 2014; Spencer et al. 2013). As FA
784 fixed cells are compatible with downstream RNA-seq analysis and ChIP studies,

785 combining proteomics on sorted cells also with these high-throughput approaches
786 would expand the in-depth analysis of gene expression (transcriptome and proteome)
787 of rare populations and/or biochemically well-defined subpopulations, such as specific
788 hematopoietic cell populations that cannot be separated on the basis of cell surface
789 markers alone.

790 **Online methods**

791 *Cell culture*

792 The NB4 cell line was originally established from acute myeloid leukemia blast
793 cells grown on bone-marrow stromal fibroblasts (Lanotte et al. 1991). NB4 cells were
794 obtained from the Hay laboratory (University of Dundee). Cells were cultured at 37 °C in
795 the presence of 5% CO₂ as a suspension in RPMI-1640 (Life Technologies)
796 supplemented with 2 mM L-glutamine, 10% v/v foetal bovine serum (FBS, Life
797 Technologies), 100 units/ml penicillin and 100 µg/ml streptomycin (100X stock, Life
798 Technologies). Cell cultures were maintained at densities between 1 x 10⁵ to 1 x 10⁶
799 cells/ml. For SILAC labeling, culture media without arginine or lysine (DCP) was
800 supplemented with either 'light' (Arg0, Lys0, Cambridge Isotope Labs) or 'heavy'
801 (Arg10, Lys8, Cambridge Isotope Labs) isotopomers of arginine and lysine. SILAC
802 labeling media was additionally supplemented with dialysed serum (10% final), 1X
803 insulin-transferrin-selenium (100X stock from Life Technologies), 1x MEM vitamins
804 (100X stock from Life Technologies), and 90 mg/L proline.

805 *Mammalian depletion and rescue experiments*

806 LLC-Pk1 cells were co-nucleofected using an Amaxa nucleofector and Mirus
807 nucleofection reagent with siRNA targeting endogenous pig TPX2 (5'
808 GAAUGGUACAGGAGGGCUU 3') and with a plasmid expressing GFP tagged si-RNA
809 resistant human TPX2, or human TPX2 with S738 mutated to either A or D.

810 Additionally, this experiment was performed using LLC-Pk1 cells expressing
811 localization and affinity purification (LAP) tagged mouse TPX2 from a bacterial artificial
812 chromosome (BAC). For generation of mutants at S738, the BAC was modified using a
813 modified LAP cassette (Poser et al. 2008). BAC DNA was nucleofected into LLC-Pk1
814 cells and selection was performed as previously described (Ma et al., 2011). Prior to use
815 in experiments, the cells were treated with siRNA to deplete endogenous pig TPX2. To
816 overexpress TPX2 constructs, 2ug of GFP-TPX2-wild type or 738A or 738D DNA was
817 nucleofected into LLC-Pk1 cells. Overexpressing cells were maintained in cell culture
818 without selection. To assay kinetochore fiber cold stability, cells were incubated in 5
819 uM MG132 for 1.5 hours to arrest cells in metaphase and then washed twice in ice cold
820 PBS, placed in ice cold culture medium for 10 minutes on ice. Cells were fixed and
821 stained for tubulin.

822 *Immunofluorescence staining*

823 NB4 cells ($\sim 0.5 \times 10^8$ cells) were washed once with phosphate-buffered saline
824 (PBS) and resuspended in freshly prepared 50 ml 0.5% formaldehyde in PBS. Cells were
825 fixed with formaldehyde for 30 min at room temperature with shaking. Cells were
826 pelleted, and permeabilised with 50 ml cold 90% methanol. Cells were then stored at -
827 20°C prior to staining.

828 Fixed, permeabilised cells were washed once with PBS and resuspended in
829 blocking buffer, 5% bovine serum albumin (BSA) in Tris-buffered saline (TBS) + 0.05%
830 sodium azide. Cells were blocked for 10 min at room temperature, pelleted, and
831 resuspended in primary antibody solution (1:200 in blocking buffer). Cells were stained
832 with primary antibody overnight at 4°C. Stained cells were then washed twice with PBS,
833 and stained with dye-conjugated secondary antibodies (1:200 in blocking buffer) for 1

834 hour at room temperature. Stained cells were washed twice with PBS, pelleted, and
835 resuspended in DAPI solution (5 µg/ml in PBS).

836 LLC-Pk1 cells were rinsed twice in room temperature PBS and fixed in
837 paraformaldehyde-glutaraldehyde fixative (3.7% paraformaldehyde, 0.1%
838 glutaraldehyde) in PBS containing 0.5% Triton X-100; fixation was carried out for 10
839 min. Microtubules were stained using a mouse anti-tubulin antibody (DM1a) or rat
840 anti-tubulin (YL ½) and appropriate secondary antibodies. Incubations with primary
841 antibodies were performed for either 1 hour at 37 C or overnight at room temperature;
842 secondary antibodies were used at room temperature for 45 min. Antibodies were
843 mixed at the appropriate final dilution with PBS containing 2% BSA, 0.1% Tween and
844 0.02% sodium azide.

845 *Flow cytometric analysis of cell cycle distribution*

846 Cells stained with either PI or DAPI were analysed on an LSR Fortessa flow
847 cytometer and data acquired using DIVA software (Becton Dickinson). DNA content was
848 evaluated based on DAPI fluorescence (measured using 355nm excitation and emission
849 at 450±50nm) or PI fluorescence (measured using 488nm excitation and emission at
850 585±42nm). Doublet discrimination was used to remove cell doublets and clumps using
851 DAPI/PI-A and DAPI/PI-W measurements. The cell cycle distribution of single (gated)
852 cells was plotted as DAPI/PI-A. Data was analysed using Flowjo software (Treestar inc.)
853 and cell cycle distributions determined using the Watson/Pragmatic model.

854 *Fluorescence Activated Cell Sorting (FACS)*

855 Immediately prior to sorting, cells were passed through a 50µm filter to remove
856 cell clumps. Cells were sorted on an Influx cell sorter (Becton Dickinson) using a 100µm
857 nozzle and sheath pressure of 20psi. Cells were distinguished from particulate material
858 on the basis of forward scatter and side scatter and single cells were identified on the

859 basis of DAPI-W v DAPI-A measurements. During sorting, data was analysed using FACS
860 Software software (Becton Dickinson).

861 *Immunofluorescence microscopy*

862 Cells purified by FACS were settled onto poly-lysine coated coverslips (BD
863 Biosciences) for 30 min at room temperature. The liquid was then carefully aspirated.
864 Cells were fixed with 2% FA in PBS for 10 min at room temperature. Cells were washed
865 twice with PBS and stained with primary antibodies for 1 hour at room temperature.
866 Cells were washed twice with PBS and stained with dye-conjugated secondary
867 antibodies for 30 min at room temperature. Cells were washed twice with PBS and
868 stained with DAPI (5 µg/ml in PBS) for 1 min at room temperature. Cells were washed
869 once with PBS and mounted in Vectashield medium (Vector Laboratories). Cells were
870 visualized using a wide-field fluorescence microscope (Zeiss, Jena, Germany; Axiovert-
871 DeltaVision Image Restoration; Applied Precision, LLC).

872 LLC-Pk1 cells were cultured in Hams F-10 mixed one to one with Opti-MEM, and
873 containing 7.5% fetal calf serum. Prior to use in experiments cells were plated on
874 22X22 mm #1.5 coverslips in 35 mm dishes or on to the surface of glass bottom petri
875 dishes (Mattek Corp). Cells were imaged using a Nikon A1R+ resonant scanning
876 confocal system equipped with a 60X NA 1.4 objective lens. For live cell imaging, cells
877 were imaged using a Nikon Eclipse TE300 or TiE equipped with a Yokagawa spinning
878 disc scan head and 100X NA 1.4 objective lens as previously described (Ma et al. 2011).
879 Image analysis was performed in ImageJ or FIJI.

880 *Cell lysis, reverse crosslinking, protein precipitation/SP3*

881 Cells were resuspended in 4% SDS in PBS, homogenised with a probe sonicator
882 (Branson, 10% power, 20 sec, 4°C), and heated to 95°C for 30 min to reverse crosslinks.
883 For MS analysis, proteins were then reduced and alkylated using TCEP (25 mM final

884 concentration, Sigma) and iodoacetamide (55 mM final concentration, Sigma). G1, S, G2,
885 and M phase lysates for the single shot analyses were then chloroform-methanol
886 precipitated. The mitotic substage fractions (G2, M, Pro, PM1, PM2, and Ana) were
887 processed using the SP3 method, as described previously (Hughes et al. 2014).
888 Phosphopeptide enrichment was performed using magnetic Ti:IMAC beads from Resyn
889 Biosciences using the manufacturer's protocol.

890 *Immunoblot analysis*

891 Lysates for SDS-PAGE analysis were prepared in lithium dodecylsulphate sample
892 buffer (Life Technologies) and 25 mM TCEP. Samples were heated to 65 °C for 5 min
893 and then loaded onto a NuPage BisTris 4 – 12% gradient gel (Life Technologies), in
894 either MOPS, or MES buffer. Proteins were electrophoresed and then wet transferred to
895 nitrocellulose membranes at 35 V for 1.5 hours. Membranes were then blocked in 5%
896 BSA in immunoblot wash buffer (TBS + 0.1% Tween-20) for 1 hour at room
897 temperature. Membranes were then probed with primary antibody overnight at 4°C,
898 washed and then re-probed with LiCor dye-conjugated secondary antibodies (either
899 IRDye-688 or IRDye-800). Primary antibodies for cell cycle immunoblot analysis were
900 obtained from Cell Signaling Technology (cyclin B1, cyclin A, cyclin E, CDT1). Bands
901 were visualized using the Odyssey CLx scanner (LiCor Biosciences).

902 *LC-MS/MS analysis*

903 Chloroform-methanol precipitated protein pellets were resuspended in 8 M urea
904 in digest buffer (100 mM Tris pH 8.0, 1 mM CaCl₂). The protein solution was then
905 diluted to 4 M urea with digest buffer and then digested with Lys-C, which was added at
906 a 1:50 w/w Lys-C:protein ratio from a 1 mg/ml stock in water (Wako Chemicals)
907 overnight at 37°C. The lysates were then further diluted with digest buffer to 0.8 M urea
908 and digested with trypsin, which was added at a 1:50 w/w trypsin:protein ratio from a

909 0.2 mg/ml stock in 50 mM acetic acid (Thermo Pierce) for four hours at 37°C. The
910 digests were then desalted using SepPak-C18 SPE cartridges, dried, and resuspended in
911 5% formic acid. Peptide concentrations were determined using the amine-reactive,
912 fluorogenic CBQCA assay (Life Technologies).

913 SP3-processed proteins were digested in a similar manner to above. For one
914 biological replicate, the resulting peptides were TMT-labelled according to
915 manufacturer's instructions. Peptides (SILAC or TMT) were then mixed, dried, and
916 resuspended in high pH reverse phase buffer A (10 mM ammonium formate in 2% ACN,
917 pH 9.3). Peptides were then chromatographed on a Dionex Ultimate 3000 off-line HPLC
918 equipped with a XBridge Peptide BEH C18 4.6 mm x 250 mm column packed with 3.5
919 µm particles containing 130 angstrom pores (Waters) and a standard gradient over 20
920 min from 25% at 0 min to 60% B at 11 min (10 mM ammonium formate in 80% ACN,
921 pH 9.3) at a flow rate of 1 ml/min. 48 fractions were collected into 24 wells in a
922 concatenated format.

923 SILAC-labelled peptides were analyzed using a Dionex RSLCnano HPLC-coupled
924 Q-Exactive Orbitrap mass spectrometer (Thermo Fisher Scientific). Peptides were first
925 loaded onto a 2 cm PepMap trap column in 2% acetonitrile + 0.1% formic acid. Trapped
926 peptides were then separated on an analytical column (75 µm x 50 cm PepMap-C18
927 column) using the following mobile phases: 2% acetonitrile + 0.1% formic acid (Solvent
928 A) and 80% acetonitrile + 0.1% formic acid (Solvent B). The linear gradient began with
929 5% B to 35% B over 220 min with a constant flow rate of 200 nl/min. The peptide
930 eluent flowed into a nanoelectrospray emitter at the front end of a Q-Exactive Plus
931 (quadrupole Orbitrap) mass spectrometer (Thermo Fisher Scientific). A typical 'Top10'
932 acquisition method was used. Briefly, the primary mass spectrometry scan (MS1) was
933 performed in the Orbitrap at 70,000 resolution. Then, the top 10 most abundant m/z

934 signals were chosen from the primary scan for collision-induced dissociation in the HCD
935 cell and MS2 analysis in the Orbitrap at 17,500 resolution. Precursor ion charge state
936 screening was enabled and all unassigned charge states, as well as singly charged
937 species, were rejected.

938 TMT-labelled peptides were analyzed using a Dionex RSLCnano HPLC-coupled
939 Tribrid Fusion mass spectrometer (Thermo Fisher Scientific). Peptides were first
940 loaded onto a 2 cm PepMap trap column (100 μ m) in 2% acetonitrile + 0.1% formic
941 acid. Trapped peptides were then separated on an analytical column (75 μ m x 50 cm
942 PepMap-C18 column) using the following mobile phases: 2% acetonitrile + 0.1% formic
943 acid (Solvent A) and 80% acetonitrile + 0.1% formic acid (Solvent B). The linear
944 gradient began with 5% B to 35% B over 220 min with a constant flow rate of 200
945 nl/min. The peptide eluent flowed into a nanoelectrospray emitter at the front end of
946 either a Q-Exactive, or Q-Exactive Plus (quadrupole Orbitrap) mass spectrometer
947 (Thermo Fisher Scientific). A max cycle time acquisition method was used (2s). The
948 primary mass spectrometry scan (MS1) was performed in the Orbitrap at 120,000
949 resolution. Then, the top N most abundant m/z signals were chosen from the primary
950 scan for CID (30%) and Rapid-mode MS2 analysis in the linear ion trap. A synchronous
951 precursor selection (SPS) method was employed. MS2 product ions were selected using
952 4 notches with a maximum injection time of 300 ms, fragmented by HCD (55%), and
953 TMT tags mass analysed in the Orbitrap at 60,000 resolution. Precursor ion charge state
954 screening was enabled and all unassigned charge states, as well as singly charged
955 species, were rejected.

956 *MS data analysis*

957 The SILAC and TMT RAW data files produced by the mass spectrometer were analysed
958 using the quantitative proteomics software MaxQuant, versions 1.5.1.2 and 1.5.3.30

959 (Cox & Mann 2008). This version of MaxQuant includes an integrated search engine,
960 Andromeda (Scheltema et al. 2011). The database supplied to the search engine for
961 peptide identifications was a UniProt human protein database ('Human Reference
962 Proteome' retrieved on April 16, 2016) combined with a commonly observed
963 contaminants list. The initial mass tolerance was set to 7 p.p.m. and MS/MS mass
964 tolerance was 20 ppm. The digestion enzyme was set to trypsin/P with up to 2 missed
965 cleavages. Deamidation, oxidation of methionine and Gln->pyro-Glu were searched as
966 variable modifications. Identification was set to a false discovery rate of 1%. To achieve
967 reliable identifications, all proteins were accepted based on the criteria that the number
968 of forward hits in the database was at least 100-fold higher than the number of reverse
969 database hits, thus resulting in a false discovery rate of less than 1%. Protein isoforms
970 and proteins that cannot be distinguished based on the peptides identified are grouped
971 by MaxQuant and displayed on a single line with multiple UniProt identifiers. The label
972 free quantitation (LFQ) algorithm in MaxQuant was used for protein quantitation. The
973 algorithm has been previously described (Cox 2014). Protein quantitation was
974 performed on unmodified peptides and peptides that have modifications that are
975 known to occur during sample processing (pyro-Glu, deamidation). All resulting MS
976 data were integrated and managed using PepTracker Data Manager, a laboratory
977 information management system (LIMS) that is part of the PepTracker software
978 platform (<http://www.PepTracker.com>).

979

Acknowledgements

This work was supported by grants to ALL from the Wellcome Trust (105024/Z/14/Z, 108058/Z/15/Z) and the EU EpiGeneSys network (Grant#: HEALTH-F4-2010-257082). We thank the UK Research Partnership Investment Fund and the Scottish Funding Council (Project H13047) for proteomics instrumentation funding and the Wellcome Trust (097418/Z/11/Z) for supporting the Flow Cytometry and Cell Sorting Facility at the University of Dundee. We thank our colleagues in the Lamond group for advice and discussion. We thank Calum Thompson and Alan Prescott (Dundee Light Microscopy Facility), the Swedlow laboratory, and Raffaella Pippa (Lamond lab) for technical advice and assistance.

Figures

Figure 1 - Lamond

An optimised workflow for intracellular immunostains and MS-based proteomics

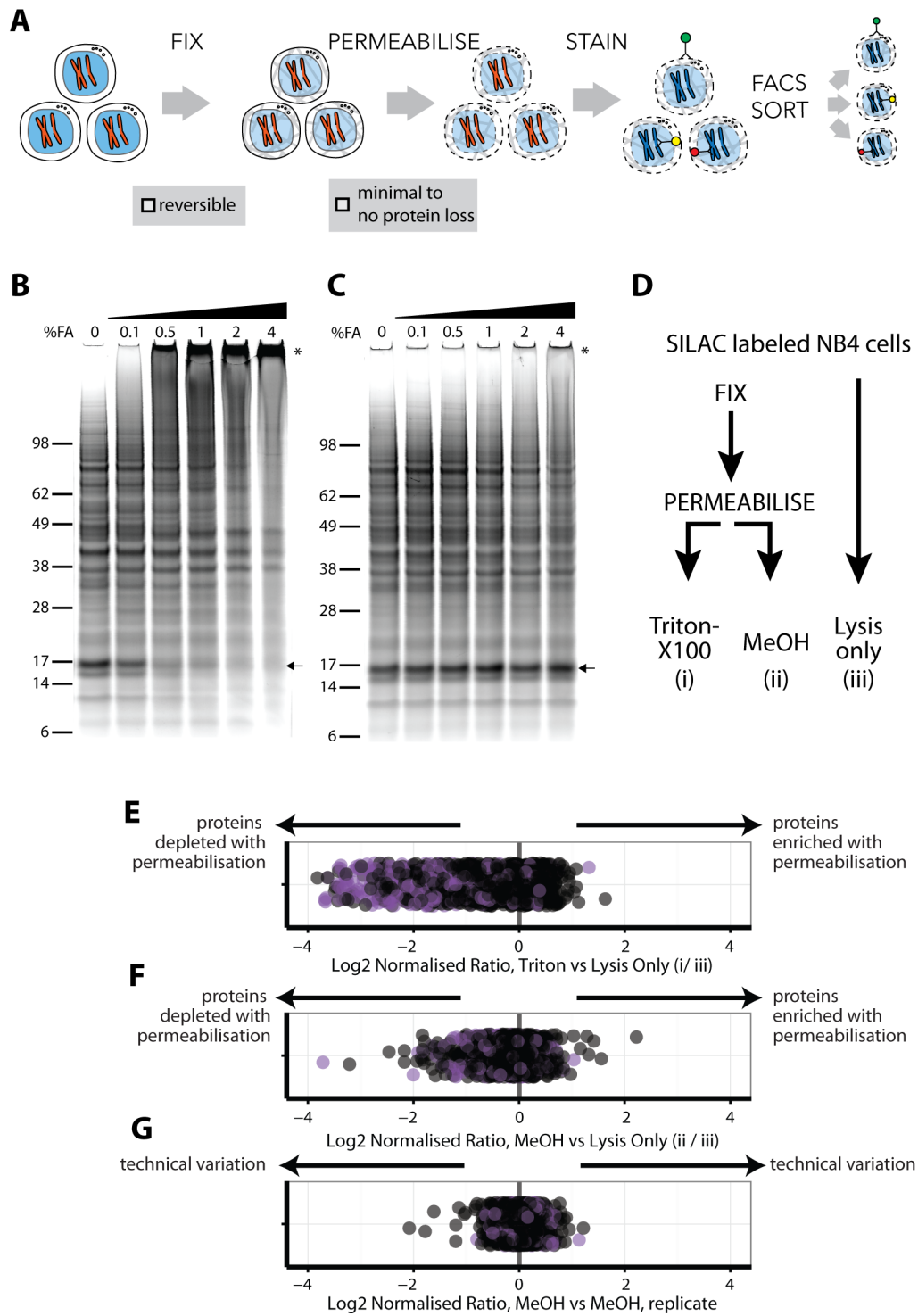


Figure 2 - Lamond

Purification of interphase and mitotic cells by FACS for MS-based proteomics

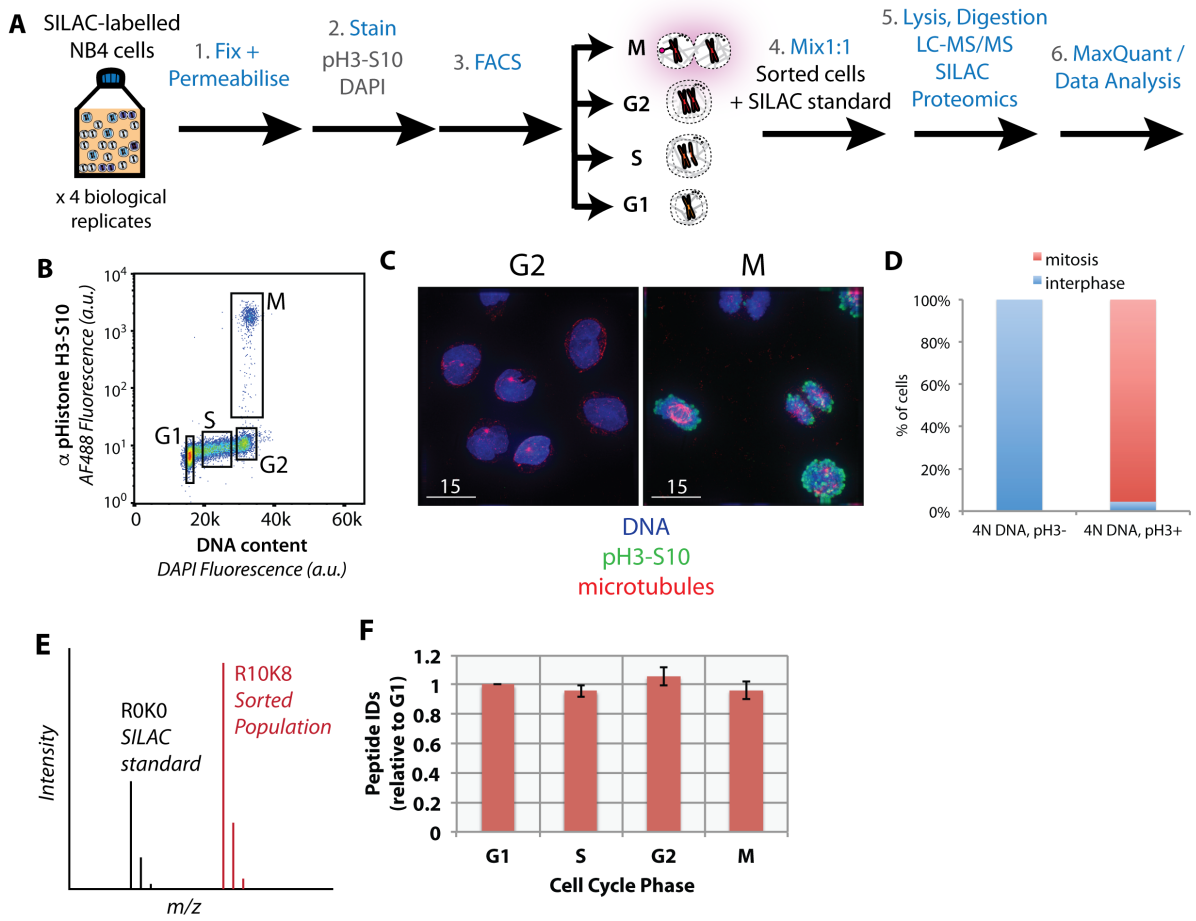


Figure 3 - Lamond

Proteomic measurement of protein accumulation across the cell division cycle

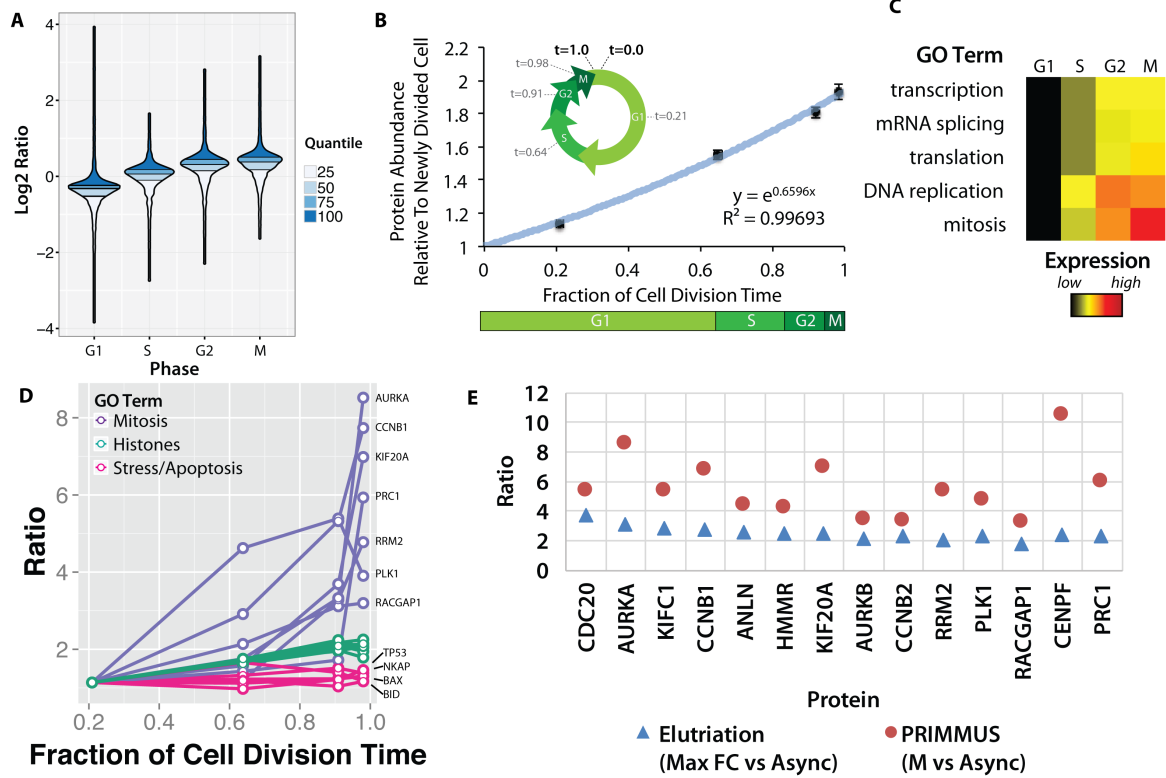


Figure 4 - Lamond

Reproducible analysis of protein phosphorylation across an unperturbed cell cycle

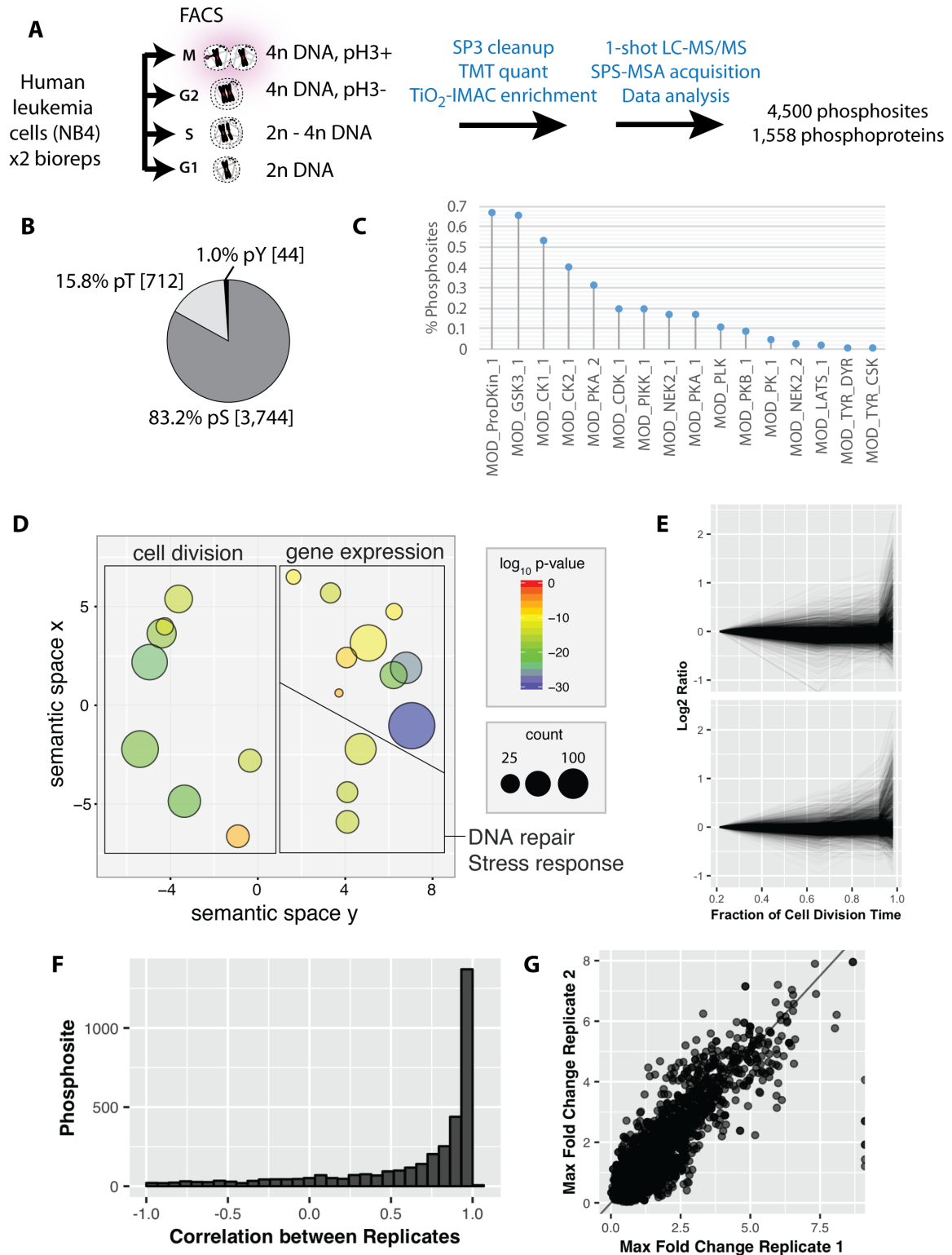


Figure 5 - Lamond
Increased global mitotic phosphorylation dominated by a subset of highly phosphorylated proteins

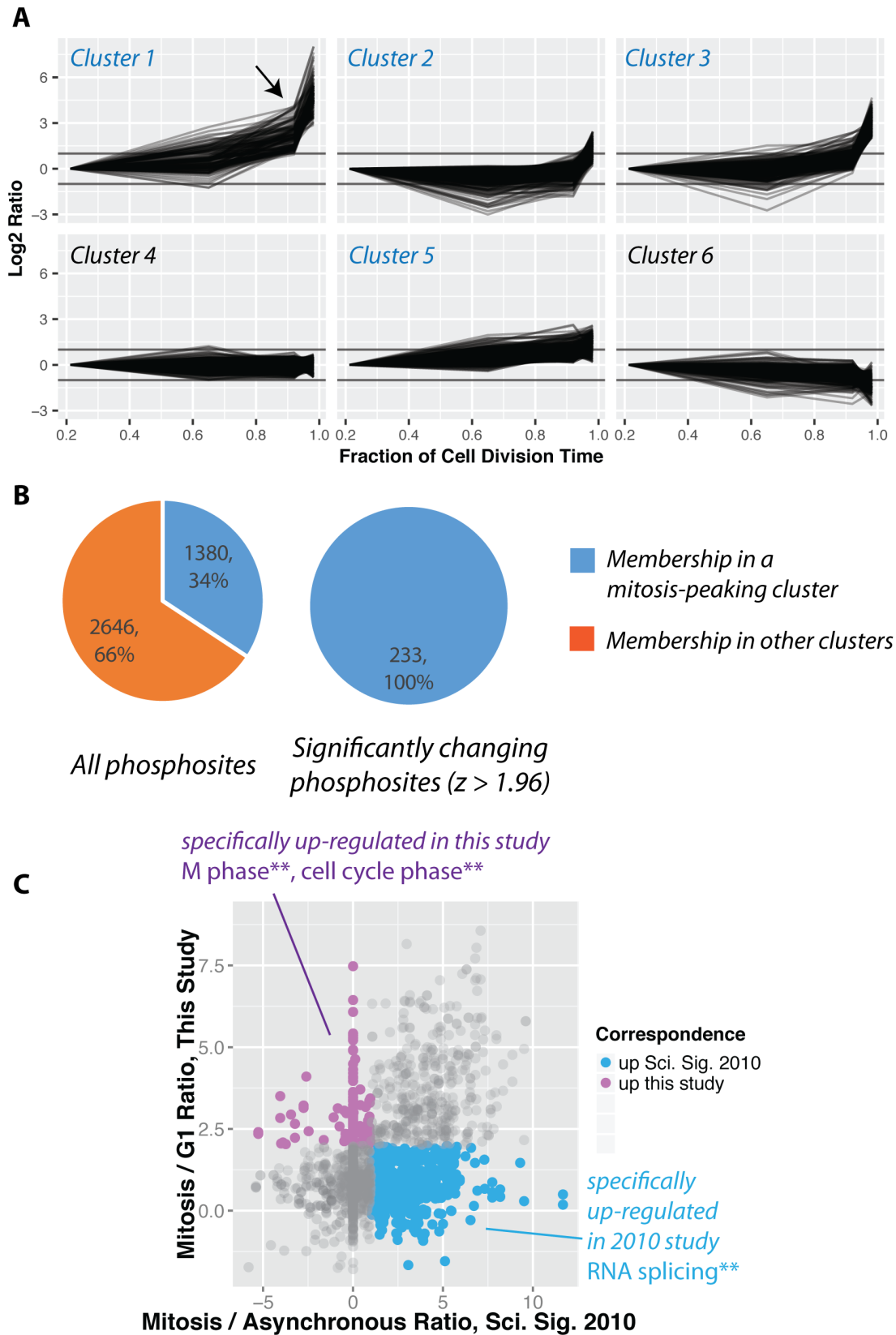


Figure 6 - Lamond

Identification of early risers, a subset of mitotic phosphorylations that begin increasing in G2 phase.

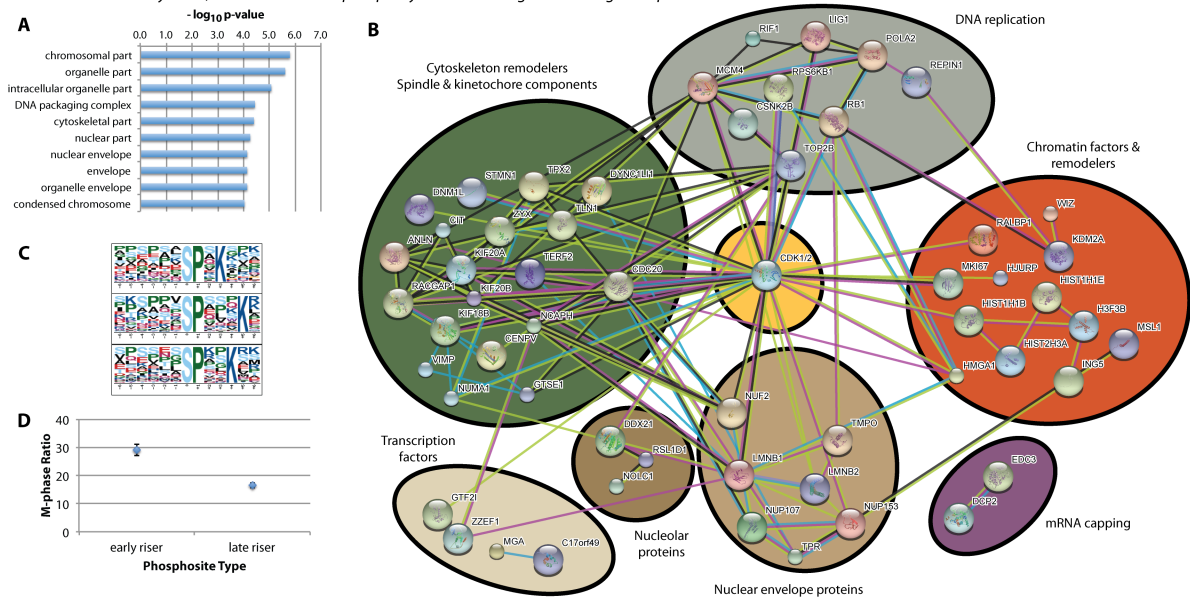


Figure 7 - Lamond

The phosphodeficient S738A mutant of TPX2 fails to rescue spindle defects induced by TPX2 depletion

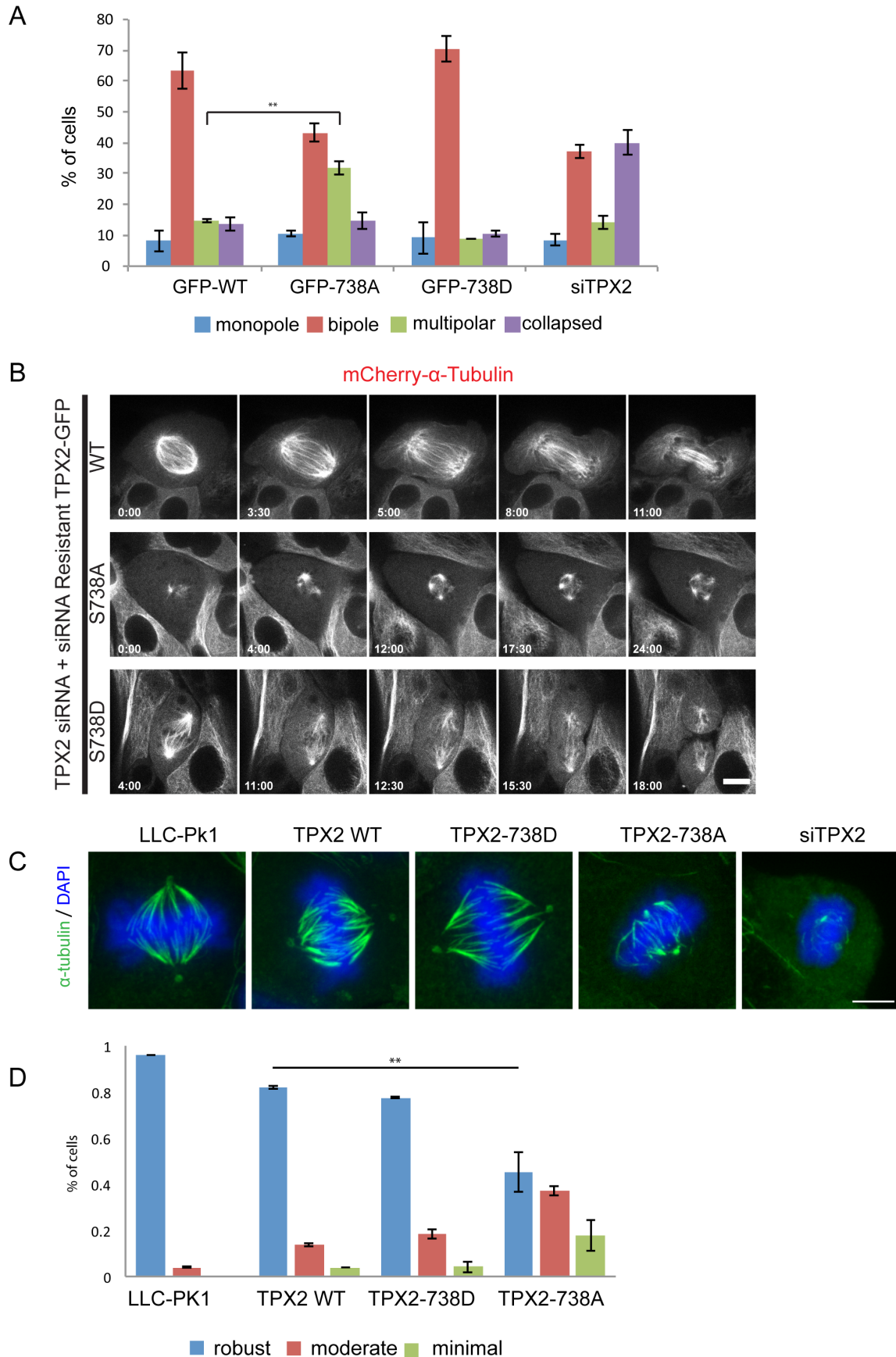


Figure 8 - Lamond
Overexpression of S738A impairs centrosome separation and formation of bipolar spindles

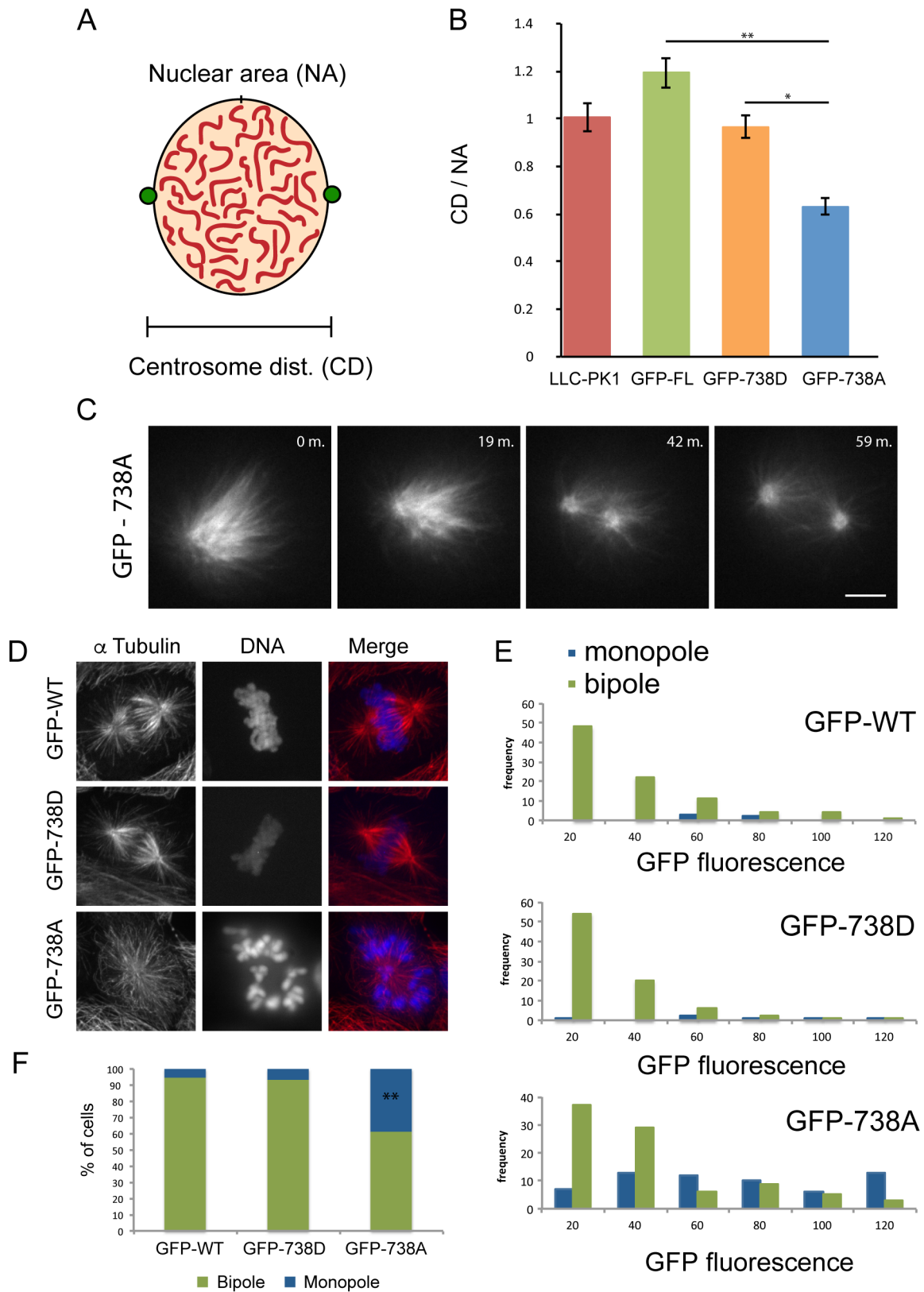


Figure 9 - Lamond
Proteome-wide analysis of protein abundance changes during mitosis

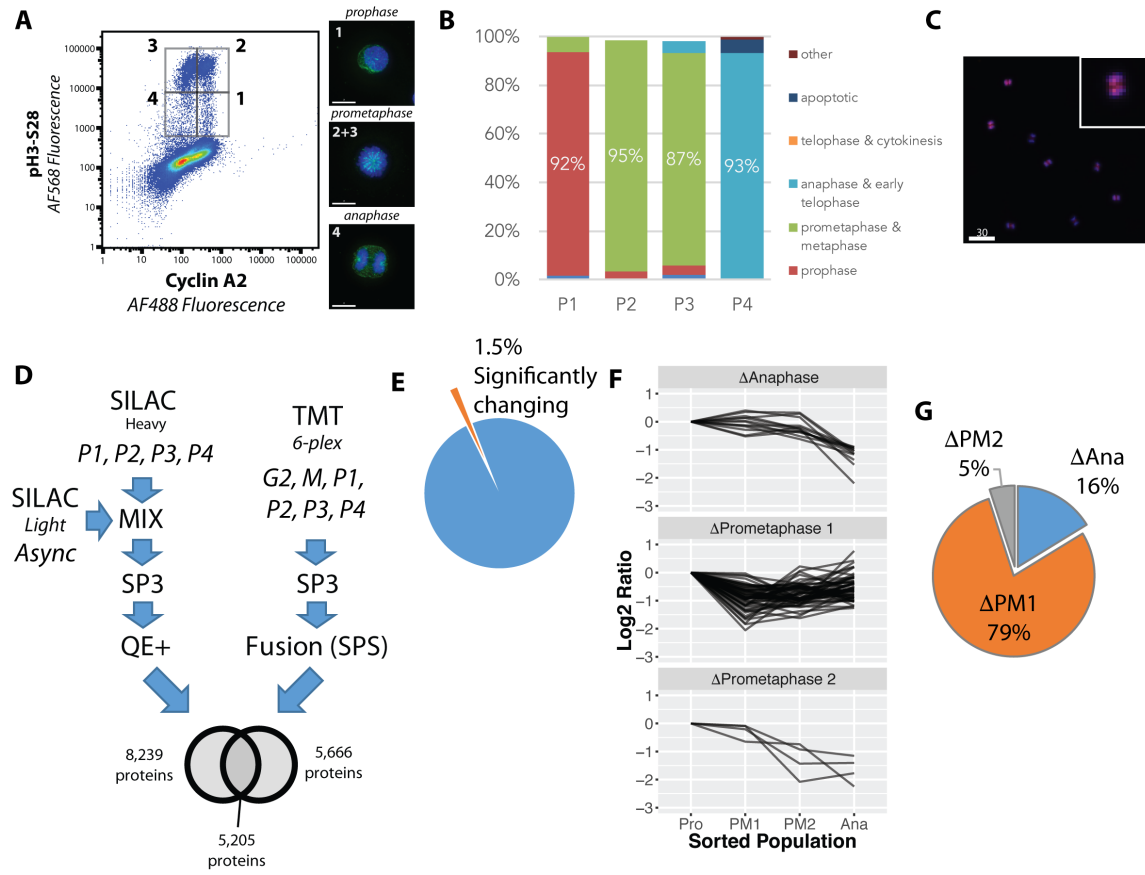


Figure 10 - Lamond

Ribonucleotide reductase M2 (RRM2) is degraded during prometaphase in a proteasome-dependent, MLN-4924 sensitive manner

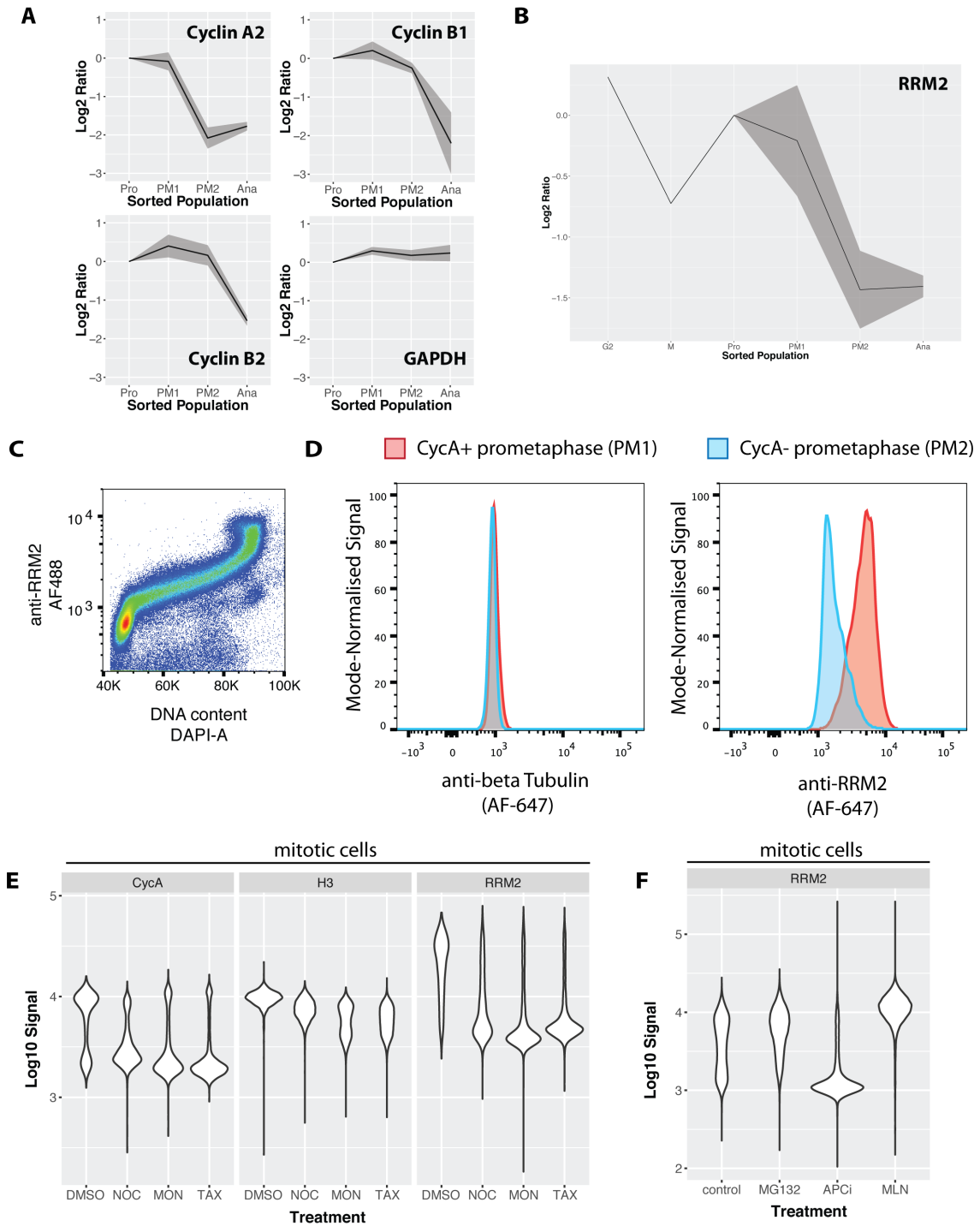


Figure Captions

Figure 1. An optimised workflow for intracellular immunostaining, FACS, and MS-based proteomics. A) An abbreviated schematic of the workflow for the Proteomics of Intracellular Immunostained Subpopulations (PRIMMUS) approach, highlighting specific steps for optimization (fixation, permeabilisation). Lysates prepared from cells crosslinked with the indicated concentrations of formaldehyde (%v/v) in PBS (B) and then de-crosslinked with heating (C) were electrophoresed by SDS-PAGE and stained for protein using Sypro Ruby. D) . SILAC labelled cells were either processed by fixation and permeabilisation, comparing 0.5% Triton X-100 (i) versus 90% methanol (ii), or with lysis only (iii). Cells were then mixed pairwise 1:1 and analysed by 'single shot' proteome workflows. The resulting SILAC ratios (e.g., H/L) are plotted as scatter plots for the pairwise comparisons, namely Triton X-100 vs. lysis only, methanol vs lysis only, and methanol versus methanol (technical replicate).

Figure 2. Purification of interphase and mitotic cells for PRIMMUS. Workflow for PRIMMUS of human leukemia cells into four cell cycle phase fractions (G1, S, G2, and M). Stained cells were sorted by FACS into four populations (G1, S, G2, and M) based on the gates shown on the pseudocolour plot in (B). The mitotic index of the M phase fraction was independently visualised by immunofluorescence microscopy and co-staining for microtubules (C) and quantitated (D). Fractions were then mixed by cell number 1:1 with an asynchronous SILAC-labelled standard and processed for 'single shot' LC-MS/MS based proteomics. The resulting measured SILAC ratios compare protein abundances in the sorted fraction versus the asynchronous standard (E). The analysis was performed with replicates (n = 4). Comparison of peptide ID rates across the sorted fractions (F).

Figure 3. Proteomic measurement of protein accumulation across the cell division cycle. (A) A 'neeps' plot showing the distribution of \log_2 SILAC ratios measured in each of the G1, S, G2, and M subpopulations in one representative replicate. The width of each 'neep' is proportional to the density, i.e. the number of proteins. Quartiles are marked by black lines, and interquartile ranges are indicated by shading. B, inset) A schematic showing the cell division cycle and the average position during the cell division cycle for each phase collected, where a newly divided cell is defined as $t = 0$, and cell division (cytokinesis) is defined as $t = 1$. B, graph) Regression analysis was performed to produce a best-fit line in the form of an exponential growth model (i.e., $y = e^{mx}$). (C) Ratios of proteins belonging to each of the indicated GO terms were averaged (mean) and visualized using a heatmap. (D) A plot of ratios of individual proteins associated with mitosis, chromatin, and the stress response versus cell cycle stage. E) A comparison of the ratio of G2&M vs. asynchronous measured in the elutriation vs. PRIMMUS datasets.

Figure 4. Reproducible analysis of phosphorylation changes across the cell division cycle. A) Workflow for phosphorylation analysis of FACS separated cell cycle states. B) Distribution of phosphorylated residues detected. C) Percentage of phosphorylation site sequences matching reported consensus substrate phosphorylation motifs (www.elm.eu.org, REF). D) Gene ontology enrichment analysis of the detected phosphoproteins (ReviGO, REF). E) Phosphorylation profiles across the

four FACS separated fractions for replicate 1 and 2. F) A histogram of correlation coefficients calculated for individual phosphorylation sites between the two replicates. G) A comparison of measured maximum fold change between replicates.

Figure 5. Increased global mitotic phosphorylation dominated by a subset of highly phosphorylated proteins. A) K-means clustering of the phosphorylation profiles. B) Distribution of mitosis-peaking phosphorylation sites, either in the entire dataset (left), or significantly changing phosphorylation sites (right). C) A comparison of phosphorylation site ratios measured in this dataset and a previous analysis of mitotic phosphorylation in human cells.

Figure 6. Identification of ‘early risers’, a subset of mitotic phosphorylations that begin increasing in G2 phase. A) Gene ontology enrichment analysis of early rising phosphorylation sites. B) A STRING network analysis of early rising phosphoproteins. Nodes with one or more connections are shown. C) Enriched sequence motifs among early rising phosphorylation sites (Motif-X). D) Comparing the M-phase ratio between ‘early rising’ and ‘late rising’ phosphorylation sites. Error bars show s.e.m.

Figure 7. The phosphodeficient S738A mutant of TPX2 fails to rescue spindle defects induced by TPX2 depletion. A) Percent of mitotic phenotypes in LLC-Pk1 cells transfected with siRNA targeting endogenous TPX2 alone or co-transfected with an siRNA resistant TPX2 construct (WT, S738A, S738D). Monopole (blue), bipole (red), multipole (green), collapsed (purple). B) Time-lapse imaging of LLC-Pk1 cells expressing mCherry- α -tubulin and co-transfected with TPX2 siRNA and siRNA resistant TPX2 constructs (WT, S738A and S738D). C) Cold stability assay. Immunofluorescence staining for MTs and DNA in parental LLC-Pk1, and cells transfected with siRNA targeting TPX2 alone or co-transfected with an siRNA resistant TPX2 construct encoding wild type (WT) TPX2, TPX2 S738A, TPX2 S738D. Maximum intensity projections of Z stacks are shown. D) Quantification of the level of cold-stable kinetochore fiber bundles shown in (C). ** P = 0.001. Scale bars in C = 5 μ m. Error Bars = St Dev. For D, N = 168, 151, 190, and 214 respectively.

Figure 8. Overexpression of S738A impairs centrosome separation and formation of bipolar spindles. A) Schematic diagram illustrating the parameters measured. B) Measurement of centrosome separation in prophase cells expressing the indicated construct. N = 20, 6, 3, and 18, respectively. C) Live cell imaging of LLC-Pk1 cell overexpressing GFP-TPX2-S738A. Initially a monopolar spindle forms that subsequently forms a bipole. GFP fluorescence. D) Spindle phenotype in cells transfected with full-length wild-type GFP-TPX2, GFP-TPX2-S738A or GFP-TPX2-S738D. E) Quantification of overexpression phenotype shown in (D). Histograms showing frequency of monopoles and bipoles binned by level of GFP fluorescence (X-axis); green - bipole, blue - monopole. F) Bar graph showing all cells scored in B; expression of TPX2-S738A results in a 4-fold increase in monopolar spindles. N = 90, 95 and 150, respectively. D) Scale bar = 5 μ m. Time in minutes in upper right. **, P < 0.001. * P < 0.05.

Figure 9. Proteome-wide analysis of protein abundance changes between mitotic subphases. A) Flow cytometry analysis of NB4 cells immunostained for pH3-S28 and CycA. Gates show populations collected by FACS. A, right) Representative light microscopy images of cell fractions. B) The frequency of each intra-mitotic stage was counted and quantified with 100 cells or more. C) Wider field of view of population 4, i.e., the anaphase-enriched population. D) Workflow for MS-based proteomic analysis involving SILAC and TMT based labelling and 3 biological replicates, resulting in 8,700 proteins identified in total. E) Pie chart indicating the percentage of significantly changing proteins (see text for criteria for significance). F) K-means clustering of profiles were qualitatively agglomerated into three groups based on subpopulation where 'trough' in abundance occurs. G) A pie chart showing the number and proportion of proteins in each protein group indicated in (F).

Figure 10. Ribonucleotide reductase M2 (RRM2) is degraded during prometaphase in a proteasome-dependent, MLN-4924 sensitive manner. A) Line graphs showing mean abundance profiles for Cyclin A2 (CycA), Cyclin B1, Cyclin B2, and GAPDH. Grey ribbons indicate 1 standard deviation from the mean. B) Mean abundance profile for RRM2. C) Flow cytometry analysis RRM2 levels vs. DNA content. D) Flow cytometry-based comparison of beta-tubulin (negative control, left) and RRM2 (right) levels in CycA+ (red) vs. CycA- (blue) prometaphase cells. E) Violin plots showing CycA, histone H3, and RRM2 levels in cells treated with either DMSO or microtubule drugs that activate the spindle assembly checkpoint (nocodazole, monastrol, taxol). F) Violin plots showing levels of RRM2 in cells treated with either vehicle control (DMSO), MG132, apcin+proTAME, or MLN4924.

Figure 11. The PRIMMUS cell cycle data is accessible through the Encyclopaedia of Proteome Dynamics (EPD). User interface features include: A) specifying type of search, including search for individual proteins, GO term, and CORUM complex membership, B) an input box for protein and other (e.g. GO term) identifiers, C) a ribbon graph showing plots for input protein identifiers (here for illustration are shown RRM2 and CCNB1) with lines indicating mean profile and ribbons indicating s.e.m., D) an interactive legend to show more information on individual proteins, and E) options to output visualisation as an SVG file or underlying data in CSV format. F) Data from other cell cycle proteomic datasets from the Lamond laboratory can be easily visualized for the same proteins using the navigation bubble map.

Figure 1 Figure Supplement 1. Immunoblot analysis of the effect of FA on the electrophoretic migration of individual proteins. Immunoblot analysis of crosslinked lysates for alpha tubulin (A) and histone H3 (B). Immunoblot analysis of crosslinked & reverse crosslinked lysates for alpha tubulin (C) and histone H3 (D). Arrowheads indicate high MW bands remaining after reverse crosslinking step that migrate at a higher MW than the expected monomer mass (arrows).

Figure 1 Figure Supplement 2. The effects of formaldehyde (FA) concentration on protein crosslinking and DNA staining. A) DNA content histograms from flow cytometry of cells fixed with the indicated concentrations of FA and using either propidium iodide (PI, left), or 4',6-diamidino-2-phenylindole (DAPI, right), as the DNA-binding dye.

Figure 10 Figure Supplement 1. siRNA-based validation of the anti-RRM2 antibody used in this study.

Akopyan, K. et al., 2014. Assessing Kinetics from Fixed Cells Reveals Activation of the Mitotic Entry Network at the S/G2 Transition. *Molecular Cell*, 53(5), pp.843–853.

Amanchy, R. et al., 2007. A curated compendium of phosphorylation motifs. *Nature Biotechnology*, 25(3), pp.285–286.

Balachandran, R.S. et al., 2016. The ubiquitin ligase CRL2 ZYG11 targets cyclin B1 for degradation in a conserved pathway that facilitates mitotic slippage. *The Journal of Cell Biology*, 215(2), pp.151–166.

Banfalvi, G., 2011. *Cell cycle synchronization: methods and protocols* G. Banfalvi, ed., New York, NY: Springer New York.

Bayliss, R. et al., 2003. Structural basis of Aurora-A activation by TPX2 at the mitotic spindle. *Molecular Cell*, 12(4), pp.851–862.

Bendall, S.C. et al., 2011. Single-Cell Mass Cytometry of Differential Immune and Drug Responses Across a Human Hematopoietic Continuum. *Science*, 332(6030), pp.687–696.

Bonardi, F. et al., 2013. A proteomics and transcriptomics approach to identify leukemic stem cell (LSC) markers. *Molecular & cellular proteomics : MCP*, 12(3), pp.626–637.

Bortner, D.M. & Rosenberg, M.P., 1995. Overexpression of cyclin A in the mammary glands of transgenic mice results in the induction of nuclear abnormalities and increased apoptosis. *Cell Growth Differ*, 6(12), pp.1579–1589.

Chabes, A.L. et al., 2003. Mouse ribonucleotide reductase R2 protein: A new target for anaphase-promoting complex-Cdh1-mediated proteolysis. *Proceedings of the National Academy of Sciences of the United States of America*, 100(7), pp.3925–3929.

D'Angiolella, V. et al., 2012. Cyclin F-mediated degradation of ribonucleotide reductase M2 controls genome integrity and DNA repair. *Cell*, 149(5), pp.1023–1034.

Di Palma, S. et al., 2011. Highly Sensitive Proteome Analysis of FACS-Sorted Adult Colon Stem Cells. *Journal of Proteome Research*, 10(8), pp.3814–3819.

Eckerdt, F. et al., Spindle Pole Regulation by a Discrete Eg5-Interacting Domain in TPX2. *Current biology : CB*, 18(7), pp.519–525.

Elzen, den, N. & Pines, J., 2001. Cyclin a Is Destroyed in Prometaphase and Can Delay Chromosome Alignment and Anaphase. *The Journal of Cell Biology*, 153(1), pp.121–136.

Endo, A. et al., 2017. The Chromatin Assembly Factor Complex 1 (CAF1) and 5-Azacytidine (5-AzaC) Affect Cell Motility in Src-transformed Human Epithelial Cells. *Journal of Biological Chemistry*, 292(1), pp.172–184.

- Floyd, S., Pines, J. & Lindon, C., 2008. APC/C Cdh1 targets aurora kinase to control reorganization of the mitotic spindle at anaphase. *Current biology : CB*, 18(21), pp.1649–1658.
- Gruss, O.J. & Vernos, I., 2004. The mechanism of spindle assembly: functions of Ran and its target TPX2. *The Journal of Cell Biology*, 166(7), pp.949–955.
- Hans, F. & Dimitrov, S., 2001. Histone H3 phosphorylation and cell division. *Oncogene*, 20(24), pp.3021–3027.
- Hein, M.Y. et al., 2015. A Human Interactome in Three Quantitative Dimensions Organized by Stoichiometries and Abundances. *Cell*, 163(3), pp.712–723.
- Hendzel, M.J. et al., 1997. Mitosis-specific phosphorylation of histone H3 initiates primarily within pericentromeric heterochromatin during G2 and spreads in an ordered fashion coincident with mitotic chromosome condensation. *Chromosoma*, 106(6), pp.348–360.
- Hrvatin, S. et al., 2014. MARIS: Method for Analyzing RNA following Intracellular Sorting. K. Aalto-Setälä, ed. *PLOS ONE*, 9(3), p.e89459.
- Hughes, C.S. et al., 2014. Ultrasensitive proteome analysis using paramagnetic bead technology. *Molecular Systems Biology*, 10(10), pp.757–757.
- Hukelmann, J.L. et al., 2016. The cytotoxic T cell proteome and its shaping by the kinase mTOR. *Cell*, 17(1), pp.104–112.
- Hutten, S. et al., 2014. A role for the Cajal-body-associated SUMO isopeptidase USPL1 in snRNA transcription mediated by RNA polymerase II. *Journal of Cell Science*, 127(Pt 5), pp.1065–1078.
- Huttlin, E.L. et al., The BioPlex Network: A Systematic Exploration of the Human Interactome. *Cell*, 162(2), pp.425–440.
- Jacobberger, J.W. et al., 2008. A new biomarker for mitotic cells. *Cytometry Part A*, 73A(1), pp.5–15.
- Juan, G. et al., 1998. Histone H3 phosphorylation and expression of cyclins A and B1 measured in individual cells during their progression through G2 and mitosis. *Cytometry Part A*, 32(2), pp.71–77.
- Kafri, R. et al., 2013. Dynamics extracted from fixed cells reveal feedback linking cell growth to cell cycle. *Nature*, 494(7438), pp.480–483.
- King, R.W. et al., 1996. How proteolysis drives the cell cycle. *Science*, 274(5293), pp.1652–1659.
- Kirkwood, K.J. et al., 2013. Characterization of native protein complexes and protein isoform variation using size-fractionation-based quantitative proteomics. *Molecular & cellular proteomics : MCP*, 12(12), pp.3851–3873.

- Klockenbusch, C. & Kast, J., 2010. Optimization of Formaldehyde Cross-Linking for Protein Interaction Analysis of Non-Tagged Integrin 1. *Journal of Biomedicine and Biotechnology*, 2010, p.13.
- Kristensen, A.R., Gsponer, J. & Foster, L.J., 2012. A high-throughput approach for measuring temporal changes in the interactome. *Nature Methods*, 9(9), pp.907–909.
- Lanotte, M. et al., 1991. NB4, a maturation inducible cell line with t(15;17) marker isolated from a human acute promyelocytic leukemia (M3). *Blood*, 77(5), pp.1080–1086.
- Larance, M. & Lamond, A.I., 2015. Multidimensional proteomics for cell biology. *Nature Publishing Group*, 16(5), pp.269–280.
- Larance, M. et al., 2016. Global Membrane Protein Interactome Analysis using In vivo Crosslinking and Mass Spectrometry-based Protein Correlation Profiling. *Molecular & cellular proteomics : MCP*, 15(7), pp.2476–2490.
- Larance, M. et al., 2013. Global subcellular characterization of protein degradation using quantitative proteomics. *Molecular & cellular proteomics : MCP*, 12(3), pp.638–650.
- Ly, T. et al., 2014. A proteomic chronology of gene expression through the cell cycle in human myeloid leukemia cells. *eLife*, 3, p.e01630.
- Ly, T., Endo, A. & Lamond, A.I., 2015. Proteomic analysis of the response to cell cycle arrests in human myeloid leukemia cells. *eLife*, 4.
- Ma, N. et al., 2010. Poleward Transport of TPX2 in the Mammalian Mitotic Spindle Requires Dynein, Eg5, and Microtubule Flux. *Molecular Biology of the Cell*, 21(6), pp.979–988.
- Ma, N. et al., 2011. TPX2 regulates the localization and activity of Eg5 in the mammalian mitotic spindle. *The Journal of Cell Biology*, 195(1), pp.87–98.
- McAlister, G.C. et al., 2014. MultiNotch MS3 Enables Accurate, Sensitive, and Multiplexed Detection of Differential Expression across Cancer Cell Line Proteomes. *Analytical Chemistry*, 86(14), pp.7150–7158.
- Mohammed, H. et al., 2016. Rapid immunoprecipitation mass spectrometry of endogenous proteins (RIME) for analysis of chromatin complexes. *Nature Protocols*, 11(2), pp.316–326.
- Nam, H.-J. & van Deursen, J.M., 2014. Cyclin B2 and p53 control proper timing of centrosome separation. *Nature Cell Biology*, 16(6), pp.538–549.
- Nelson, D.M. et al., 2002. Coupling of DNA synthesis and histone synthesis in S phase independent of cyclin/cdk2 activity. *Molecular and Cellular Biology*, 22(21), pp.7459–7472.
- Neumayer, G. et al., 2014. TPX2: of spindle assembly, DNA damage response, and cancer. *Cellular and Molecular Life Sciences*, 71(16), pp.3027–3047.

- Nordlund, P. & Reichard, P., 2006. Ribonucleotide Reductases. *Annu. Rev. Biochem.*, 75(1), pp.681–706.
- Olsen, J.V. et al., 2010. Quantitative Phosphoproteomics Reveals Widespread Full Phosphorylation Site Occupancy During Mitosis. *Science Signaling*, 3(104), pp.ra3–ra3.
- Ong, S.-E. et al., 2002. Stable Isotope Labeling by Amino Acids in Cell Culture, SILAC, as a Simple and Accurate Approach to Expression Proteomics. *Molecular & Cellular Proteomics*, 1(5), pp.376–386.
- Ozlu, N. et al., 2015. Quantitative comparison of a human cancer cell surface proteome between interphase and mitosis. *The EMBO Journal*, 34(2), pp.251–265.
- Poser, I. et al., 2008. BAC TransgeneOmics: a high-throughput method for exploration of protein function in mammals. *Nature Methods*, 5(5), pp.409–415.
- Pozarowski, P. & Darzynkiewicz, Z., 2004. Methods in Molecular Biology: Checkpoint Controls and Cancer, Volume 2. In A. H. Schönthal, ed. *Analysis of Cell Cycle by Flow Cytometry*. Humana Press, pp. 301–311.
- Robbins, E. & Borun, T.W., 1967. The cytoplasmic synthesis of histones in hela cells and its temporal relationship to DNA replication. *Proceedings of the National Academy of Sciences of the United States of America*, 57(2), pp.409–416.
- Rønning, O.W., Pettersen, E.O. & Seglen, P.O., 1979. Protein synthesis and protein degradation through the cell cycle of human NHIK 3025 cells in vitro. *Experimental cell research*, 123(1), pp.63–72.
- Sackton, K.L. et al., 2014. Synergistic blockade of mitotic exit by two chemical inhibitors of the APC/C. *Nature*, 514(7524), pp.646–649.
- Sawin, K.E. et al., 1992. Mitotic spindle organization by a plus-end-directed microtubule motor. *Nature*, 359(6395), pp.540–543.
- Scharff, M.D. & Robbins, E., 1965. Synthesis of ribosomal RNA in synchronized HeLa cells. *Nature*, 208(5009), pp.464–466.
- Smith, E. et al., 2011. Differential control of Eg5-dependent centrosome separation by Plk1 and Cdk1. *The EMBO Journal*, 30(11), pp.2233–2245.
- Soucy, T.A. et al., 2009. An inhibitor of NEDD8-activating enzyme as a new approach to treat cancer. *Nature*, 458(7239), pp.732–736.
- Spencer, S.L. et al., 2013. The proliferation-quiescence decision is controlled by a bifurcation in CDK2 activity at mitotic exit. *Cell*, 155(2), pp.369–383.
- Sullivan, M. & Morgan, D.O., 2007. Finishing mitosis, one step at a time. *Nature Reviews Molecular Cell Biology*, 8(11), pp.894–903.
- Sutherland, B.W., Toews, J. & Kast, J., 2008. Utility of formaldehyde cross-linking and

- mass spectrometry in the study of protein–protein interactions. *Journal of Mass Spectrometry*, 43(6), pp.699–715.
- Thompson, A. et al., 2003. Tandem Mass Tags: A Novel Quantification Strategy for Comparative Analysis of Complex Protein Mixtures by MS/MS. *Analytical Chemistry*, 75(8), pp.1895–1904.
- Toews, J. et al., 2008. Mass spectrometric identification of formaldehyde-induced peptide modifications under in vivo protein cross-linking conditions. *Analytica chimica acta*, 618(2), pp.168–183.
- Trieselmann, N., 2003. Ran modulates spindle assembly by regulating a subset of TPX2 and Kid activities including Aurora A activation. *Journal of Cell Science*, 116(23), pp.4791–4798.
- van Zon, W. & Wolthuis, R.M.F., 2010. Cyclin A and Nek2A: APC/C-Cdc20 substrates invisible to the mitotic spindle checkpoint. *Biochemical Society transactions*, 38(Pt 1), pp.72–77.
- Vos, J.W. et al., 2008. The plant TPX2 protein regulates prospindle assembly before nuclear envelope breakdown. *The Plant Cell*, 20(10), pp.2783–2797.
- Wang, T. et al., 2015. Identification and characterization of essential genes in the human genome. *Science (New York, N.Y.)*, 350(6264), pp.1096–1101.
- Wheeler, R.J., 2015. Analyzing the dynamics of cell cycle processes from fixed samples through ergodic principles. *Molecular Biology of the Cell*, 26(22), pp.3898–3903.

Supplementary Tables

Supplementary Table 1. The effect of fixation and permeabilisation protocols on MS-based protein quantitation. A tab-delimited text file containing a list of all the protein groups identified with ≥ 2 peptides per protein group and their associated SILAC ratios comparing the different fixation and permeabilisation protocols.

Supplementary Table 2. Analysis of protein accumulation across interphase and mitosis. The table consists of an excel file containing two worksheets. The first worksheet lists the protein groups identified with ≥ 2 peptides per protein group and their associated SILAC ratios in four biological replicates. For each biological replicate, the ratios were normalised to the ratio measured in G1. An offset was then added to the G1 ratio to account for the difference in time between cell division and an average G1 cell (calculated from Figure 5B). The second worksheet also lists the same protein groups, but with the unnormalised ratios. These are the ratios that were used to produce the 'neeps' plot in Figure 5A.

Supplementary Table 3. Analysis of protein phosphorylation across interphase and mitosis. The table consists of a tab-delimited file containing the phosphorylation sites measured, quality measures (PEP, Score), and TMT ratios calculated relative to the G1 fraction from the two biological replicates. B – biological replicate, fc – fold change, repcor – Pearson's correlation score between the ratio patterns of the two biological replicates

Supplementary Table 4. Analysis of protein abundances during mitotic subphases. The table consists of a tab-delimited file containing the proteins identified, quality measures (Q-value, Score, number of peptides), TMT ratios calculated relative to the prophase fraction, and SILAC ratios calculated relative to the prophase fraction in biological duplicate. cor – Pearson's correlation score between the ratio patterns of the three biological replicates (only mitotic subphases are compared). numcor – number of times the Pearson's correlation score is greater than 0.